To the Graduate Council:

I am submitting herewith a thesis written by Yiqun Pan entitled "Processing of Ceramic Matrix Composite Using Microwave Energy." I have examined the final copy of this thesis for form and content and recommend that it be accepted in partial fulfillment of the requirements for the degree of Master of Science, with a major in Metallurgical Engineering.

Thomas T. Meek

T.T. Meek, Major Professor

We have read this thesis
and recommend its acceptance:

Carl J. McHargue

R. A. Buchanan

Accepted for the Council:

C. W. Minkel

Associate Vice Chancellor
and Dean of The Graduate School

STATMENT OF PERMISSION TO USE

In presenting this thesis in partial fulfillment of the requirement for a Master of Science degree at The University of Tennessee, Knoxville, I agree that the Library shall make it available to borrowers under rules of the Library. Brief quotations from this thesis are allowable without special permission, provided that accurate acknowledgement of the source is made.

Requests for permission for extensive quotation from or reproduction of this thesis in whole or in parts may be granted by the copyright holder.

Signature Yiqun Pan

Date Nov. 24, 1992

Processing of Ceramic Matrix Composite Using Microwave Energy

A Thesis

Presented for the

Master of Science

Degree

The University of Tennessee, Knoxville

Yiqun Pan

December 1992

DEDICATION

This thesis is dedicated to my husband, Dr. Xiao Zhang. I hope he knows how much he is loved and appreciated.

ACKNOWLEDGMENTS

I would like to thank my major professor, Dr. T. T. Meek, for his guidance and patience. In the course of this thesis research, a number of other scholars have assisted me generously. In particular I am indebted to Professor R. A. Buchanan and Professor C. J. McHargue for their advice and direction as well as their review of the manuscript. Great appreciation is also expressed to Professor C. R. Brooks, Dr. P. F. Becher, and Mr. T. N. Tiegs for their useful discussion. I am grateful to Dr. W. A. Simpson, Dr. J. Dunlap, and Mr. R. Williams for their invaluable help during my research work.

Special gratitude is expressed to Third Millenium Technologies, Inc. for supplying silicon carbide whiskers. I also would like to express my thanks to Aluminum Company of America for supplying alumina powders.

Finally, and most of all, I wish to thank my husband, Dr. Xiao Zhang, for his encouragement, insight, and unceasing support throughout the duration of this project.

ABSTRACT

Studies of microwave processing of a ceramic composite were conducted on alumina reinforced by silicon carbide whiskers (10 vol%). The processing was accomplished with an industrial microwave heating system. Analyses were performed by mechanical testing methods, and by modern microanalysis methods including electron microscopy (scanning electron microscopy, transmission electron microscopy with energy-dispersive spectroscopy), X-ray photoelectron spectroscopy, and X-ray diffraction.

The results indicated that microwave sintered silicon carbide whisker reinforced alumina matrix composite has an improvement of fracture toughness over conventionally sintered monolithic alumina. Crack deflection along the whiskers was the major toughening mechanism operating in the composite. Also, whisker bridging, whisker debonding, and whisker pullout all contributed to the improvement of fracture toughness of the composite. Grain-bridging toughening was also observed.

The microstructure study showed that the interfacial bonding between the whiskers and the alumina matrix played an important role in the composite materials. The TEM study revealed that an amorphous interphase existed at the whisker-matrix interface. Strong interface interactions between the whiskers and the alumina matrix weakens the benefits of the whisker toughening effects. The samples sintered at 1650°C showed a 10% higher toughness than those sintered at 1550°C where a strong interface interaction was

obvious.

It was found that ultrafine grain size was a characteristic of the microwave sintered composite, which is directly related to the microwave internal volumetric sintering mechanism.

The investigation also showed that without using sintering aids there was an amorphous layer on most of the alumina grain boundaries although the sintering temperature was 400 to 500°C lower than the melting temperature of the alumina. This observation provided direct evidence of the decrease of local melting temperature at the grain boundary area due to the effects of capillary and electromagnetic field.

TABLE OF CONTENTS

CHAPTER	PAGE
I. INTRODUCTION.	1
II. BACKGROUND.	3
Microwave Processing of Ceramics.	3
Ceramic Matrix Composite (CMC) Materials.	16
III. EXPERIMENTAL PROCEDURES.	31
Fabrication of the Ceramic Matrix Composite.	31
CMC Property Measurements.	38
Characterization of CMCs.	46
IV. RESULTS AND DISCUSSION.	50
Raw Materials.	50
CMC Properties.	56
CMC Structures and Phases.	68
CMC Toughening Mechanisms.	82
Characteristics of Microwave Sintering of CMCs. . .	92
Conclusions.	93
BIBLIOGRAPHY.	95
VITA.	105

LIST OF FIGURES

FIGURE PAGE

2.1. Heating patterns in conventional and microwave furnaces. 4

2.2. (a) Random dipole orientation in an uncharged capacitor, (b) Dipole ordering by a constant electric field, $E_{applied}$ (adopted from [7]). 6

2.3. Interaction of microwaves with materials (adopted from [11]) 10

2.4. Schematic of twist of a crack around rods of two aspect ratios, R, at constant volume fraction (adopted from [57]). 19

2.5. A schematic diagram of crack bridging mechanism operative in a whisker reinforced ceramic matrix composite (adopted [55]). 22

2.6. Schematic diagram of major toughening mechanisms of CMCs. 24

3.1. Flow chart of preparation procedures of green samples. 33

3.2. Schematic diagram of the microwave applicator. 35

3.3. Schematic diagram of the microwave sintering system. . 36

3.4. (a) Typical power curves in the 2.45 GHz microwave furnace for sintering of Al_2O_3-10 vt% SiC_w CMC at 1650°C for 30 min. Pf is the forward energy, Pb is the backward (non-coupled) energy, (b) the corresponding temperature profile. 39

FIGURE PAGE

3.5. Schematic diagram of the flaw pattern induced by Vickers indentation. 43

3.6. Plot demonstrating the correlation between toughness values determined by indentation and by conventional means. 44

4.1. SEM micrograph of AG-16 Al_2O_3 powders used as the matrix material. 51

4.2. General morphology of SiC whiskers used as the reinforcement material. 52

4.3. Typical irregular shaped whiskers: (a) nobbled, (b) microfaceted, and (c) pine cone shaped. 53

4.4. Stacking faults on {111} plane of the whisker. The inset shows the selected area diffraction pattern. 55

4.5. Amorphous layer on the surface of the whisker. The inset shows the microdiffraction pattern of the amorphous layer. 57

4.6. The survey spectrum XPS analysis of the as-received SiC whisker surface. 58

4.7. Silicon 2p spectrum of the surface of the as-received SiC whisker surface. 59

4.8. (a) TEM bright field image of the Al_2O_3 grains of the CMC sintered at 1650°C for 20 min, (b) corresponding TEM dark field image showing amorphous layers surrounding the Al_2O_3 grains. 63

FIGURE PAGE

4.9. Occasionally, lateral cracks occurred in some of the indentation, which is unacceptable for toughness measurement. 65

4.10 Examples of plot of $P/c_0^{3/2}$ over working range of load P for tested CMCs for which well-defined radial cracks could be obtained. 67

4.11. Optical micrograph of a typical structure of Al_2O_3-10 vt% SiC_w composite. 69

4.12. TEM bright field image of a SiC whisker bonded with the alumina matrix through an amorphous interphase. The inset shows the selected area diffraction pattern of the interphase region with a typical amorphous diffraction feature. 70

4.13. TEM dark field images of alumina grain boundaries surrounded by amorphous layers: Samples were sintered at (a) 1650°C and (b) 1550°C, respectively, for 20 min. Note that the melting point of alumina is 2045°C. 71

4.14. A dislocation array located at a small angle grain boundary of alumina matrix. 73

4.15. SEM fractograph of the specimen sintered at 1550°C for 30 min. Note that there is no or very small grain growth under microwave sintering condition. 74

FIGURE PAGE

4.16. Abnormal grain growth was occasionally observed. . . . 75
4.17. Small pores were found in some of the abnormally grown alumina grains. 77
4.18. Amorphous interphases exist in whisker-matrix interface of CMCs. Samples were sintered at (a) 1650°C and (b) 1550°C, respectively, for 20 min. 78
4.19. Results of EDX microanalysis across the interphase region for the samples sintered at two different temperatures. 79
4.20. An example of XRD pattern of the microwave sintered CMC. Note the existence of a small amount of β-Al_2O_3 phase. 81
4.21. SEM micrographs show cracks deflected around the SiC whiskers. (a) A crack was deflected by about 40° along a whisker lying on the polished surface; (b) a crack was deflected along the edge of the whisker oriented perpendicular to the polished surface. 83
4.22. SEM micrograph shows a whisker debonded from the matrix as the result of the crack propagation. 84
4.23. SEM micrograph shows a whisker was bridged across the crack. 85
4.24. SEM micrograph shows the existence of grain bridging across the crack, a matrix self-toughening mechanism. . 86

4.25. SEM fractographs of the fracture surfaces of the CMCs. Samples were sintered at (a) 1650°C and (b)1550°C, respectively, for 30 min. 87

4.26. SEM fractographs show the whisker-pull-out phenomenon. Samples were sintered at (a) 1650°C and (b)1550°C, respectively, for 30 min. 88

4.27. SEM fractograph shows crack deflection along the SiC whisker edges. 90

4.28. (a) SEM fractograph of a whisker cluster which was apparently the origin of the crack; (b) an enlarged view of the whisker cluster. 91

LIST OF TABLES

TABLE		PAGE
3.1.	Characteristics of SiC whiskers.	32
4.1.	SiC whisker surface atomic fraction (at%) vs. binding energy (BE).	56
4.2.	Density and porosity of the composite.	60
4.3.	Hardness and Young's modulus of the composite.	62
4.4.	Fracture toughness measured by indentation method. .	68

CHAPTER I

INTRODUCTION

Advancement of modern technology leads us into a new era of development of high performance materials. Ceramic composite materials have been extensively studied as a direct result of the growing market for reliable high-technology structural ceramics. One of the important categories of the ceramic composites is the whisker-reinforced ceramic-matrix composite. The whisker reinforcement provides remarkable improvements of fracture toughness (initially an intrinsic obstacle for the high-tech application), impact and creep strength of the composite relative to the unreinforced matrix which is susceptible to catastrophic failure by fast growth of a single dominant crack.

The processing methods of whisker reinforced ceramic matrix composites include conventional sintering, hot processing, and newly emerged microwave sintering. The development of industrial microwave heating technology is starting to enter the various ceramic processing areas. The unique advantages of fast sintering, high density, and improved material properties make it superior in certain respects to other processing methods.

Microwave sintering of ceramic composites, especially whisker reinforced ceramic composites, has not been studied extensively, particularly with regard to the relation between properties and microstructures in the micron to sub-micron range. In addition, the mechanism of microwave interaction with ceramics has also not yet

been fully understood. Based on the best knowledge of the author, currently there is no transmission electron microscopy (TEM) study of microwave sintered ceramic materials. The whisker reinforcement mechanism for microwave sintered ceramic composites needs further study.

The purpose of this study was to develop a microwave sintering method to process silicon carbide whisker-reinforced alumina matrix composites in an industrial microwave heating system. Using mechanical testing methods and modern microcharacterization techniques, the study placed emphasis on the relationship between the properties and the microstructures of the composite. The whisker reinforcement mechanism was explored. In addition, the microwave-ceramic interaction was studied in this ceramic composite system.

CHAPTER II

BACKGROUND

2.1 Microwave Processing of Ceramics

2.1.1 Introduction

During the last decade, the development of microwave technology for industrial heating processes has had an impact on ceramic processing although this technology still is in its infancy. The driving force to develop this technique stems from its inherent advantages--rapid processing cycles, capability of developing new and unique microstructures, and high economic efficiency [1-4].

Microwave sintering of ceramics uses the dielectric mechanism of nonmetallic materials. In the microwave sintering/heating process, electromagnetic energy is absorbed throughout the volume of a material and converted into heat; therefore, the material is heated uniformly without gradients in temperature. This leads to more uniform shrinkage upon sintering and to uniform microstructure. Obviously, this internal and volumetric heating is reverse of the heating of materials processed by conventional heating where heat is transferred to the surface of the material first by conduction, convection, and/or radiation, and then into the interior mainly by thermal conduction. The differences in the sintering/heating mechanisms for these two methods are graphically shown in Figure 2.1.

Based on the rules of the Federal Communication Commission (FCC), presently available microwave frequencies for industrial

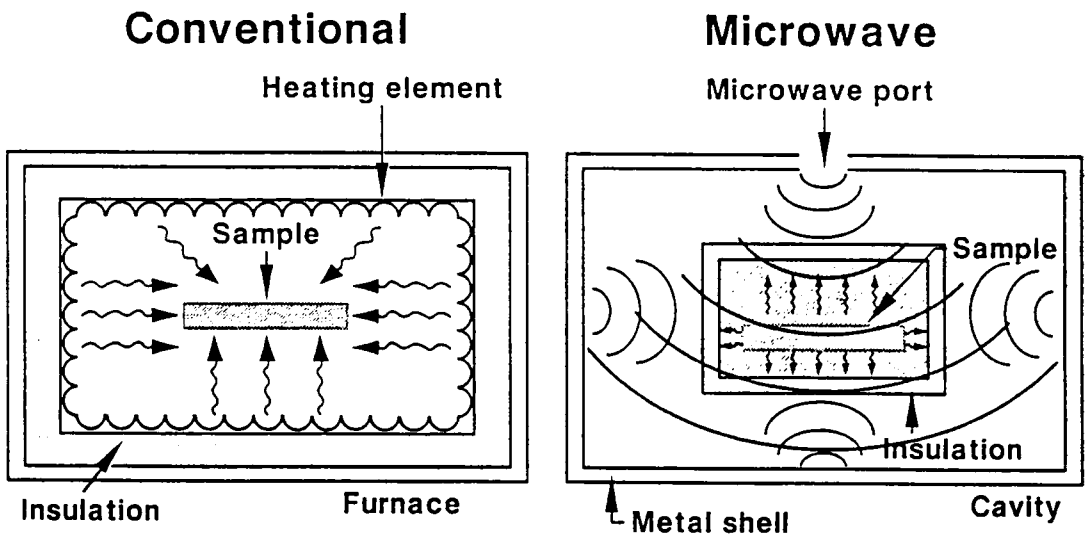

Figure 2.1 Heating patterns in conventional and microwave furnaces (adopted from [11]).

application in the United State are basically 0.915 and 2.45 GHz. Recently, in order to develop a better understanding of microwave energy-material interactions, high frequency microwave equipment has been used in a few research groups, such as the 28 GHz microwave furnace at Oak Ridge National Laboratory (ORNL) [3] and the 60 GHz furnace at Los Alamos National Laboratory (LANL) [2].

2.1.2 Dielectric Mechanisms

The mechanisms responsible for the internal heat generation capability of microwave sintering/heating are based on the dielectric properties of the material, which includes dipolar polarization (orientation), ionic conduction, various magnetic losses, interface polarization, molecule twisting and bending, and a number of resonance phenomena. For processing of many ceramic materials with electromagnetic energy in the frequency range 10 MHz $< f <$ 3 GHz, the first two mechanisms are the most important and dominant [5].

The orientation polarization of a dielectric material occurs when the molecules with displaced positive and negative charges of equal magnitude (dipoles) orient themselves in a direction opposite to an applied electric field (Figure 2.2). The alignment of the dipoles results in a reduced internal electric field as compared to the applied field. The dipoles will attempt to rotate through an angle of 180° each time the applied field changes direction. The molecules away from an equilibrium position with respect to the applied field results in energy taken up by the dipoles. This energy is retained as stored potential energy while the field remains. If the applied field is

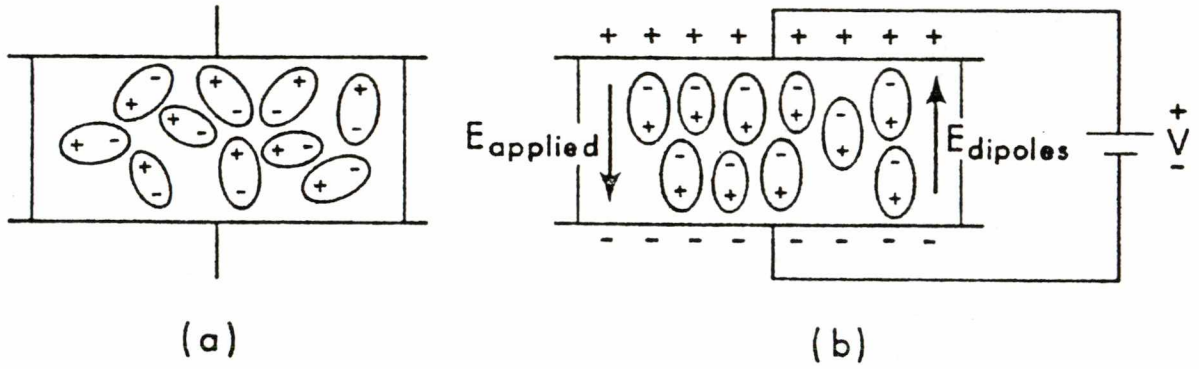

Figure 2.2 (a) Random dipole orientation in an uncharged capacitor, (b) Dipole ordering by a constant electric field, $E_{applied}$ (adopted from [7]).

removed, the dipoles relax to a new equilibrium position, and the energy is released as random kinetic energy which is returned to the system in the form of heat. Coupled with this orientation polarization effect, a dielectric also can be heated through direct conduction due to, for example, the redistribution of charge particles under the influence of the externally applied electric field forming conducting paths. This process is particularly important in mixtures of heterogeneous materials [6].

Parameters affecting dielectric behavior

The complex dielectric constant (ε^*) and the loss tangent ($\tan \delta$) are usually used to describe the dielectric behavior of materials. The expressions of these terms are written as

$$\varepsilon^* = \varepsilon' - j\varepsilon'' \tag{2.1}$$

and

$$\tan \delta = \frac{\varepsilon''}{\varepsilon'} = \frac{\sigma}{2\pi f \varepsilon'} \tag{2.2}$$

where ε' is the dielectric constant, ε'' is the loss factor, σ is the electrical conductivity caused by conduction and displacement current, and f is the radiation frequency. The real part of ε^* directly influences the amount of energy that can be stored in a material in the form of electric fields, whereas the imaginary part of ε^* is a direct measure of how much energy a material can dissipate in the form of heat. The value of the loss tangent determines the degree of absorption of microwaves by a dielectric material. The greater the

polarization of the material, the greater will be the dielectric constant and the quantity of energy that can be stored in the material [6].

The dielectric constant is a function of many variables including radiation frequency, temperature, composition, etc. Among these, the frequency parameter is probably the most basic one. Von Hipple first demonstrated that the loss characteristics of oxide materials vary as a function of microwave frequency [8]. Walton studied the effect of changing temperature on the relative dielectric constant (ε_r) ($\varepsilon_r = \varepsilon''/\varepsilon_0$; $\varepsilon_0 = 8.84 \times 10^{-12}$ F/m, the dielectric constant of free space) and loss tangent ($\tan \delta$). The results showed that both parameters increase with the increment of temperature [9]. Ho thought that this is due to an increase in the polarizability caused by volumetric expansions [10]. Because of the complexity of the interactions of materials with microwave radiation, experimental dielectric measurement and subsequent theoretical data extrapolation are still under study in various groups.

2.1.3 Classification of Ceramic Materials in Electromagnetic Field

As mentioned above, the ability to absorb energy by ceramic materials in the microwave field depends entirely on the dielectric loss--the dissipation of microwave energy in materials. In order to distinguish their heating/sintering capability, ceramic materials are classified as three types:

(1) Transmitting materials: Microwave radiation passes through materials such as boron nitride, silica, calcia, magnesia, alumina, and yttria much like sunlight shining through a window without any energy loss. Therefore, a low loss tangent is the characteristic of this

group of materials. As a result, these materials are very difficult to sinter at ambient temperature under low radiation frequency. This group of materials is also called non-coupling or non-absorbing materials.

(2) Absorbing materials: Zirconia, silicon carbide, and hafnia belong to so-called absorbing materials due to their large loss tangent values and hence large energy absorbing ability. The penetration depth of the microwave radiation depends on the power and the frequency.

(3) Reflecting materials: For reflecting materials, microwave radiation is generally reflected from the materials, as similar to the way a ball would bounce off a wall. The most distinguished example of a reflecting material is graphite. Figure 2.3 shows the three different types of interactions discussed above.

Although some materials like magnesia, alumina, and yttria do not readily absorb microwave energy at ambient temperature (and therefore are called transmitting materials), they do absorb and couple somewhat when heated from 500 to 1000°C. This change is mainly due to the dramatic changes in dielectric properties (especially the loss tangent) at higher temperatures. The ability of a material to couple with the microwave field also can be greatly enhanced by adding conductive or magnetic phases in the form of fibers, particles, or other additives. In these materials, the conductive or magnetic phases will absorb microwave energy far more rapidly than the matrix, and hence, will be heated selectively and rapidly [11].

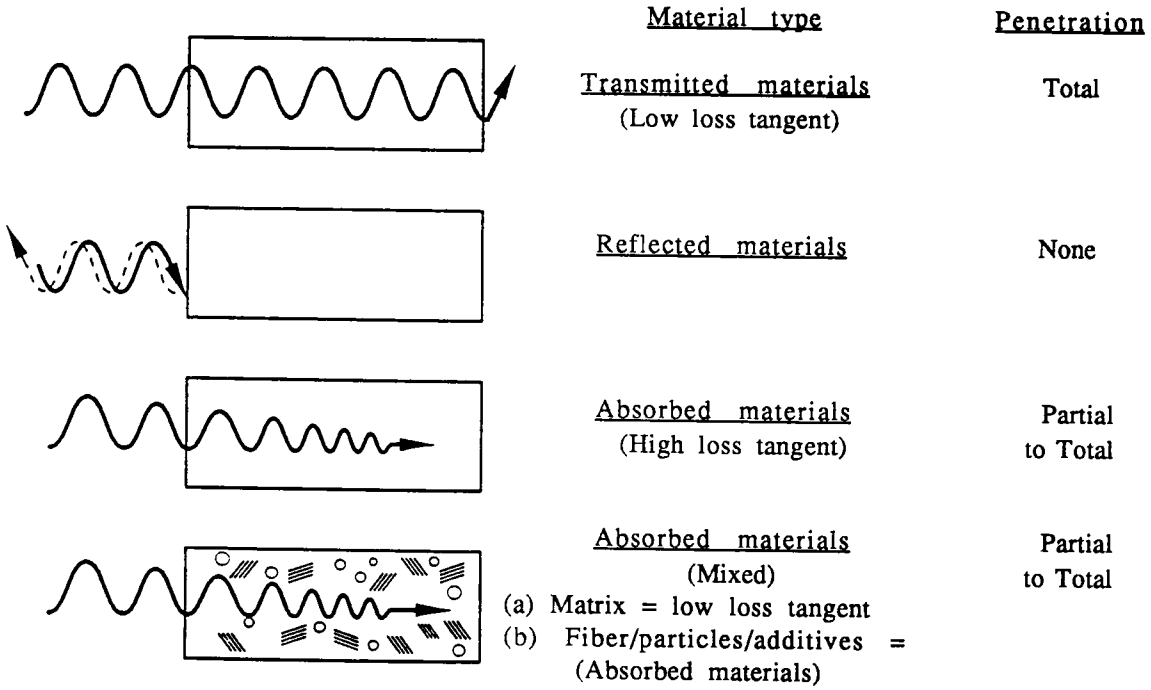

Figure 2.3 Interaction of microwaves with materials.

2.1.4 Microwave Processing of Ceramic Materials

The advantages of microwave processing of ceramic materials have caused the continuous development of this technique in both theoretical and technical aspects in various material systems.

Theoretical aspects and proposed modeling

The theory of interactions between incident electromagnetic radiation and ceramic materials has not yet been well established, although some progress has been made. Major physical parameters which can be used to describe the effects of the interaction of a dielectric with microwave energy are power dissipated and power penetration depth.

(1) power dissipated

Microwave sintering/heating involves the conversion of electromagnetic energy into heat. Energy is transported through space or any medium by means of electromagnetic waves. The power dissipated by a ceramic dielectric in an electric field can be calculated from the well-known relation [11]

$$P = 2\pi f \varepsilon' \tan\delta \, |E|^2 \qquad (2.3)$$

where E is the magnitude of the internal electric field strength (V/m).

Eqn. (2.3) shows that the ceramic must have an appreciable loss tangent and dielectric constant in order for significant heating to occur. The higher the frequency the smaller the electric field required for a specific power dissipation, assuming the loss factors are of similar magnitude. Similarly for a material with low loss

factor, the sinterability could be increased by increasing the frequency. For example, by processing at 28 GHz instead of 2.45 GHz, approximately 25 times more power can be dissipated in high-purity alumina [1].

(2) penetration depth

The penetration depth (D) is defined as the distance D that incident microwave energy decreases to 1/e (which is equal to 37%) of the original field strength. The penetration depth is calculated by the following formula [11]:

$$D = \frac{3\lambda_0\varepsilon_0}{8.686\pi\tan\delta\sqrt{\varepsilon'}} \qquad (2.4)$$

where λ_0 is the incident or free-space wavelength.

Eqn.(2.4) shows that a lower frequency results in a greater penetration depth. Heating does not necessarily increase, since the internal field E could be low, depending on the properties of the material [12]. Normally, for high-purity alumina and high loss tangent material silicon carbide, the penetration depths are of the order of meters and micrometers, respectively, for 2.45 GHz microwave radiation at room temperature.

For further understanding how a material interacts with a microwave field, different models have been proposed by several investigators [13-18]. It has been suggested that the enhanced densification observed in microwave sintering is caused by the preferential interaction of the microwaves with the pore-solid interface, which leads to particle surfaces that are "hotter" than the particle interiors [13]. Another view is that the "microwave effect" is

similar to that observed for plasma sintering of materials [14], in which the particle surface is also somehow activated. The "microwave effect" exists due to interactions between the microwaves and the bulk material (including grain boundaries), which accelerates diffusional process in some as yet to be defined manner [15].

A new mechanism based on theoretical analysis and experimental observation has been suggested by Meek and Zhang [16], and may provide a reasonable explanation for the observed "apparent lower activation energy" reported by Janney and Kimrey [19]. Using a surface thermodynamic analysis, it was found that the presence of an electromagnetic field may decrease the melting temperature of an intergranular capillary region by as much as several hundred degrees in the case of alumina. Experimental results are consistent with this suggestion. Amorphous surface layers have been found in microwave sintered samples, but not in conventional sintered samples, although the sintering temperatures are the same (in the solid state sintering region). There exists either a transient or a permanent liquid phase during the microwave sintering process at the apparent solid state sintering temperature. A preliminary sintering model has also been proposed. This observation provides a unique explanation for the observed high density and rapid sintering rate of microwave sintered oxide materials.

Numerical modeling techniques have become powerful tools for quantitative analysis of the microwave-material interaction and its effects on the diffusion process during sintering as well as for

simulating temperature distributions in samples in the microwave field [20-24].

Application

Initial studies were concentrated on ceramics which couple strongly with the incident radiation. More recently, there has been a trend toward studying materials with particular relevance to modern engineering ceramic applications. Some of these latter ceramics have very low dielectric loss at room temperature, meaning that the material is essentially transparent to microwave radiation. However, at 800-1000°C most of these ceramics are sufficiently "lossy" to continue heating of their own accord. Considerable attention has, therefore, been focussed on finding methods to achieve the initial heating of low-loss ceramics, which includes the use of susceptors, additives, and high frequency radiation.

The earliest work aimed at generating high temperatures in ceramic materials using microwave radiation was performed in 1967 by Ford and Pei [25]. Up to the present, researches have mainly focused on identifying and understanding the properties of ceramics sintered with microwave energy, which includes microwave/material interactions and their effects on sintering processes, quantification of the mechanisms, key material parameters controlling dielectric response, determination of heat and mass transport mechanisms, and sintering of various types of ceramics and composites [4]. Many material systems including uranium oxide, barium titanium, ferrite, alumina, alumina-silicon carbide composites, boron carbide, titanium diboride, zirconia, and glass-ceramics, among others, have been

investigated in the microwave environment [2, 26-33]. Among them, the sintering behaviors of alumina and zirconia have been studied in more detail than any of the other systems [11]. The short sintering cycle and higher density are the distinguishing characteristics compared to conventional sintering. It has also been reported that the apparent activation energy of microwave sintering is one-third that of conventional sintering [19]. The large difference in the sintering rate was thought to be due to high diffusion rates induced by the microwave field [19, 34].

Magnetic oxides such as ferrites have been rapidly sintered in microwave fields, and the physical and magnetic properties were comparable with those of conventionally sintered ferrites [29, 35]. Krage indicated that in addition to dielectric losses, magnetic losses were also operative at temperatures below the Curie point [29].

For $YBa_2Cu_3O_{7-x}$ superconductor, sintering and annealing in microwave energy shows improved oxygen content in the superconducting phase. This is attributed to the coupling of CuO with microwave energy. The onset of the superconductive transition occurs at 93 K compared to 90 K for the conventional material. The internal heating of CuO leads to an improved microstructure with less porosity [36].

The covalently bonded carbides and nitrides are not effectively densified by conventional pressureless sintering, without the addition of sintering aids. However, the improved densification can be achieved by using microwave radiation either with or without sintering aids [30, 37].

2.2 Ceramic Matrix Composite (CMC) Materials

2.2.1 Introduction

Monolithic ceramic materials in general have a very attractive package of properties, exhibiting relatively high strength, stiffness and hardness, corrosion resistance, and high temperature stability. However, the application potentials are impeded by their brittle nature--low toughness, and other effects, such as insufficient reliability--due to poor fracture characteristics, low thermal-stress resistance as a result of high thermal expansion and elastic moduli.

The fracture toughness (K_{Ic}) or critical stress intensity factor characterizes the resistance to crack propagation and is considered to be a material property. Explorations of a variety of approaches to enhance the fracture toughness have been prompted during the last decade. Discrete particles (ZrO_2, TiC, and TiB), fibers (SiC, C), and whiskers (SiC and B_4C) [38-42] are incorporated into ceramic matrices to block the crack propagation so that the ceramic matrix composites (CMCs) could meet the challenge from the requirement of advanced structural materials.

2.2.2 Major Toughening Mechanisms

Since the first toughening mechanism, transformation toughening, was proposed by Garvie et al, [43], a number of models and methods, based on experimental studies and theoretical deductions, have been devised to explain the processes that might yield ceramics with increased fracture toughness values by the use of a second phase in the matrix [44]. These toughening mechanisms can be divided into two major categories: (1) process zone

mechanisms which include transformation toughening and microcracking toughening, and (2) bridging mechanisms which include ductile particle reinforcement, grain bridging, fiber/whisker bridging, crack pinning, crack deflection, and pullout of the reinforcing phase [44-47]. Additionally, many of these mechanisms may be combined in a given material to enhance the toughening effects [48].

In a composite system reinforced by whiskers, the most encountered toughening mechanisms contributed by the whiskers are microcracking, crack deflection, and whisker bridging. In addition, whisker pullout, although limited in extent, accompanies the eventual failure of the bridging whiskers [49-52].

Microcracking

Microcracks occur within regions of local residual tension, and may be caused by thermal expansion mismatch and/or by transformation [53-54]. The microcracks also occur along the lowest energy paths and locally relieve the residual tension. Furthermore, the microcracks reduce the elastic modulus within the microcracking process zone [55]. The basic material quantities which allow microcracking (residual stresses and low fracture energy interfaces) also lead to grain bridging. Often, microcracking and bridging operate simultaneously, the relative contributions depending on features of the microstructure.

The crack shielding caused by microcracking may be separated into dilational and modulus contributions. The dilational contribution to K_{tip} (stress intensity factor) from the residual stress field has the

same form as that associated with transformations and thus depends on both zone size and shape of the process zone [55]. The modulus contribution, however, depends only on the zone shape [54]. Limitations on the analysis of microcrack toughening exist due to a poor fundamental understanding of the degradation caused by microcracks directly ahead of the crack front and limited knowledge of the interactions between the modulus and dilational contributions.

Crack deflection

A second phase or a whisker located in the near tip field of a propagating crack perturbs the front, causing a reduction in the stress intensity. The reduced stress intensity depends on the character of the whisker shape and volume fraction [56] as well as the nature of the crack interaction. The crack, upon interaction with the whisker, will tilt along the whisker/matrix interface by a certain angle out of its original plane of propagation, i.e., the crack deflection is a non-planar crack. Deflection toughening arises whenever interaction between the crack front and the minor phase produces a non-planar crack, subject to a stress intensity lower than that experienced by the corresponding planar crack. The non-planar crack arises either from residual strains present in the material or from the existence of weakened interfaces. However, it has been found that the residual strain has no significant influence on the magnitude of crack interaction toughening. Figure 2.4 schematically illustrates the crack deflected situation by rods (second phase material) with different aspect ratios.

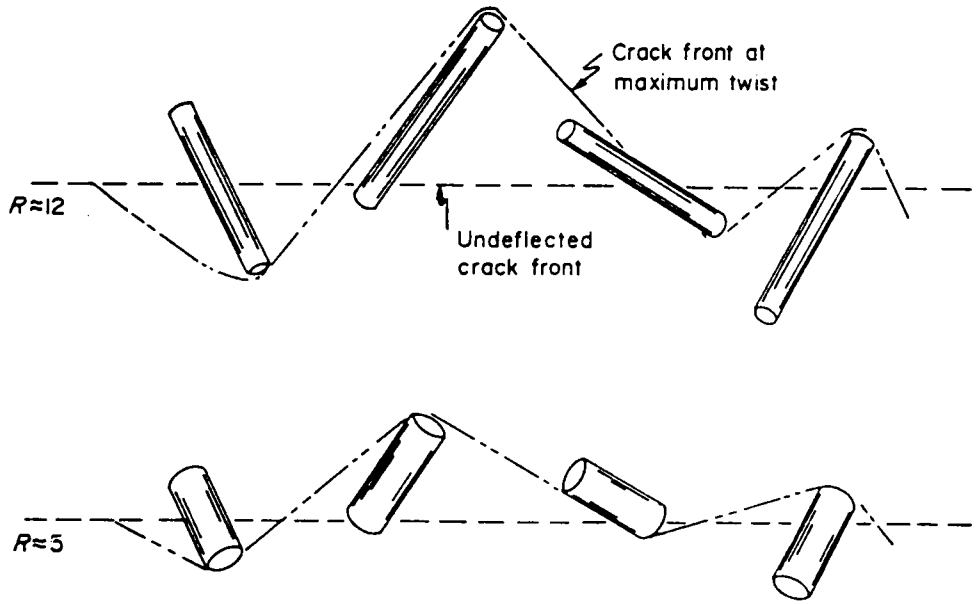

Figure 2.4 Schematic of twist of a crack around rods of two aspect ratios, R, at constant volume fraction (adopted from [57]).

Crack bridging

Another mechanism which can lead to an increase in toughness has been termed "crack bridging". This refers to the toughening by bridging which is induced by debonding along the whisker/matrix interfaces [58]. The debonding allows the whisker to remain intact within a small bridging zone behind the crack [58, 59]. The propagation of a dominant crack [56] entails four stages of energy dissipation that contribute to higher toughness, described in the equation below,

$$\Delta G_c/fd \approx S^2/E - E\, e_T^2 + 4\,(\Gamma_i/R)/(1 - f) + (\tau/d) \sum_i (h_i^2/R) \qquad (2.5)$$

where, ΔG_c is the strain energy release rate, f the whisker volume fraction, d the extent of interface debonding, S the strength of the reinforcing element, E the elastic modulus of the composite, e_T the misfit strain in tension at the whisker/matrix interface, Γ_i the fracture energy of the interface, R the radius of cross-section of reinforcing elements, τ the sliding stress at the whisker/matrix interface, and h_i the pullout length.

The first term in Eqn. (2.5) is the strain energy stored in the whisker before it fractures. This energy is dissipated in the form of acoustic waves during the propagation of cracks, thus contributing favorably to fracture toughness of the composite.

Due to the difference in the thermal expansion coefficients of the matrix and the whisker, there is misfit strain at the whisker/matrix interfaces in the composites. The second term in the

Eqn. (2.5) reflects the loss of residual misfit strain energy caused by matrix cracking and debonding at the interface. Residual tensile stress at the interface causes undesirably extensive debonding at the crack wake, while residual compressive stress facilitates controlled debonding depending further on the sliding friction coefficient, μ, and the surface morphology of the whisker. The misfit strain must be small ($< 3 \times 10^{-3}$) and preferably compressive, normal to the interface.

When a crack propagates through the composite, the whiskers that intersect the crack plane and do not fracture bridge the crack, and lead to debonding at the whisker/matrix interface near the crack wake (Figure 2.5). The debonding results in the creation of new fracture surface area. Some of the energy of the propagating crack is converted into fracture surface energy. The process of debonding and the generation of new fracture surfaces are expressed in the third term of the equation. There are several requirements for the debonding to occur effectively. The fracture energy, Γ_i, of the interface must be sufficiently low to prevent stress concentration at the interfaces and for the propagation of the crack to be relatively smooth and extensive. A stronger whisker with a fracture surface energy higher than that of the interface will divert the crack along the interface rather than across the whisker. Thus the bridging action of the whisker is realized.

After debonding has taken place at the interface, the whiskers that do not fracture immediately are likely to be pulled out of the matrix to an extent dictated by the sliding frictional coefficient in the

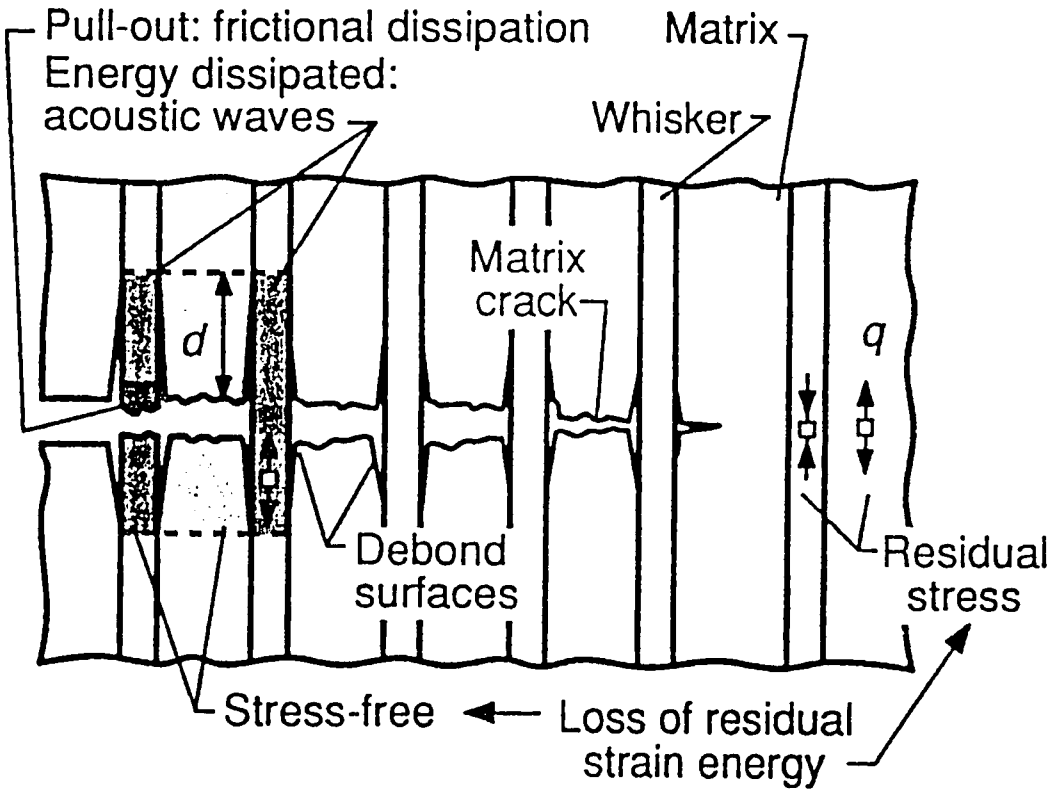

Figure 2.5 A schematic diagram of crack bridging mechanism operative in a whisker reinforced ceramic matrix composite (adopted [55]).

debonded interface. A lower frictional coefficient produces a larger pullout length, h_i, thus contributing more favorably to the fracture toughness of the composites. A large pullout length also means that the likelihood of stress concentration at the interface is low thereby preventing possible catastrophic failure of the whiskers. Reinforcements with lower sliding frictional coefficients, i.e. morphologically smooth whiskers, are generally produced by coating the whiskers with carbon or boron nitride, which have proven to reduce the sliding stress at the interfaces and to increase the pullout length considerably [60].

Figure 2.6 is a schematic illustration of the major toughening mechanisms for CMCs.

Among these toughening mechanisms, crack deflection is ostensibly governed only by whisker shape and volume fraction [57], albeit that the relative elastic moduli and thermal expansion coefficients also may have implicit effects on the deflection path. Conversely, the whisker bridging and pullout depend sensitively upon the mechanical properties of the interface, the whisker strength/toughness, the whisker radius, and volume fraction [56]. From the composite material design point of view, it has been clear that in order that a particular whisker and matrix will combine to form a successful composite with increased toughness, three basic factors must be considered:

(1) the difference between the coefficient of thermal expansion of the whisker (CTE_w) and that of the matrix (CTE_m), (2) the elastical moduli (E) of matrix and whisker, and (3) the chemical compatibility

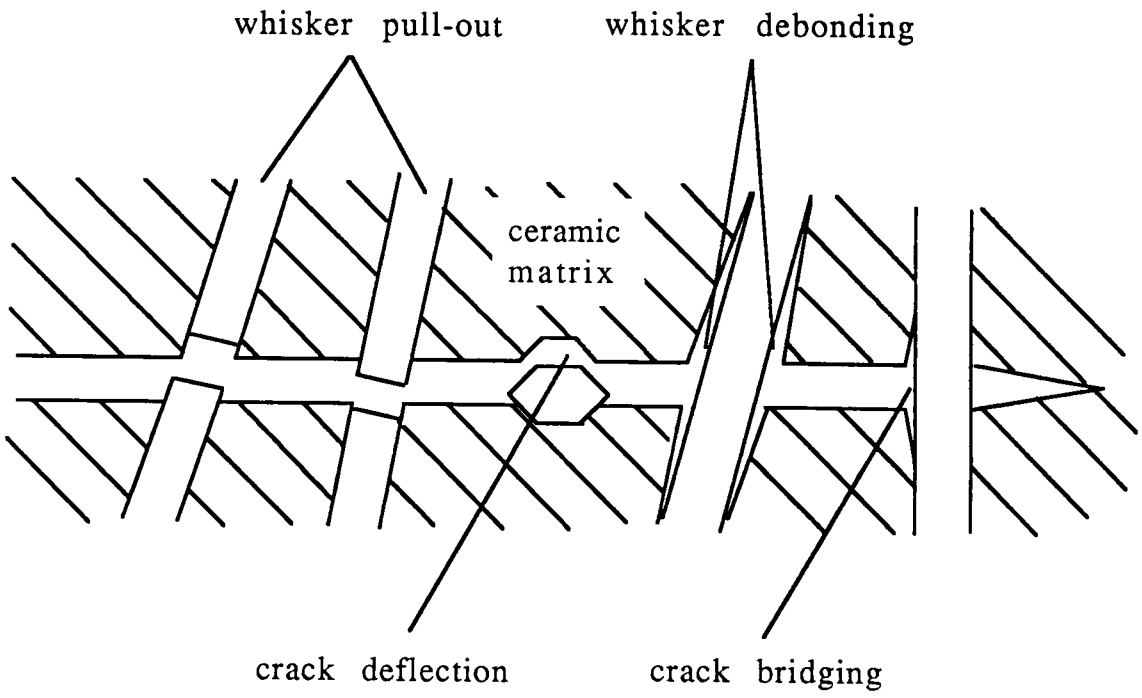

Figure 2.6 Schematic diagram of major toughening mechanisms of CMCs.

between the whisker and matrix at the processing temperature. In the case of applying SiC_w into the Al_2O_3 matrix, $CTE_w < CTE_m$, and the matrix is under tangential tension and the whisker under compression. If sufficient tensile stresses develop in the matrix, microcracking may occur to further absorb cracking energy and enhance K_{Ic}.

2.2.3 Silicon Carbide Whisker-Reinforced Alumina Matrix Composite (SiC_w-Al_2O_3)

A number of studies have investigated the effects of incorporating SiC whiskers in an Al_2O_3 matrix. The first principal objective of the previous studies were focused on the room-temperature fracture toughness and fracture strength of the composites. The initial study of SiC_w-Al_2O_3 composite was made by Becher and Wei [41]. They used hot pressing (HP) as the consolidation technique and incorporated 20 vol% SiC_w into the Al_2O_3 matrix. The composite substantially increased the fracture toughness, K_{Ic} = 8.7 $MPam^{1/2}$, over that of the Al_2O_3 (matrix) alone, while it retained the flexural strength, σ_f = 800 MPa. An important observation in their studies was that the SiC whiskers were reoriented during hot pressing with the long axis of the whiskers being perpendicular to the direction of the applied pressure. The whisker preferential orientation resulted in anisotropic mechanical properties of the composite.

During the last several years, the research areas of the SiC_w-Al_2O_3 composite can be described mainly in three directions: (1) fabrication techniques which included studies of different sintering

techniques and improvement of green sample preparation [61, 62], (2) microstructure characterization, including interface effects [63], and (3) mechanical behavior analysis which included studies of fatigue, creep, erosion, thermal shock, fracture toughness, and flexure strength [49, 50, 64-67].

Fabrication techniques

The fabrication of whisker-reinforced ceramic composites generally involves starting with raw materials (powder and whisker) and some mixing technique. Then the mixture is first consolidated either as a loose powder in a shaped mold, an extruded solid with aqueous or organic binders, or a compact form by cold pressing. Final consolidation into a monolithic article then involves the application of heat, such as conventional sintering or microwave sintering techniques, or a combination of elevated temperature and pressure, which normally is the hot pressing (HP) technique.

The mixing of powders (Al_2O_3) with whiskers (SiC_w) is the first step of the fabrication. Deagglomerate of whisker "nets" and the matrix powders as well as the dispersion of whiskers in the matrix were considered as basic parameters of preparation of qualified green samples. The study of dispersion techniques has been carried out by several different investigators [62, 68-71]. Because of the formation of a constraining network of whiskers [61, 72], SiC whisker-containing Al_2O_3 powder compacts are difficult to densify. This network usually exerts tensile stresses on the matrix and severely inhibits particle rearrangement and shrinkage during sintering [61, 73]. In order to enhance densification in whisker-

containing powder compacts, three methods were employed: (1) adding additives, such as MgO/Y_2O_3, which forms a liquid phase at the sintering temperature [61] (the liquid phase enhances densification through rearrangement processes and/or increases in diffusion coefficients, which improves the mass transport rate), (2) lowering the aspect ratio of the SiC whiskers and/or using smaller Al_2O_3 particles, which would increase the packing efficiency and improve the green density [61], and (3) increasing the densification of green samples, which is related to the techniques of dispersing whiskers into the matrix and preparation of the green samples as discussed above.

Interface effects

Based on the current understanding of whisker reinforcement, the composite mechanical properties are dominated by the interface. A weak bond must be placed at the interface to facilitate debonding and to decrease sliding resistance for the composite to have attractive mechanical behavior [55]. The degree of chemical and/or mechanical bonding at the whisker/matrix interface should be considered as the major factor that influences the toughness of the composite. Tiegs et al used a series of different commercial SiC whiskers as reinforcing materials to test the effect of surface chemistry on the fracture toughness [66]. They found that high oxygen content on the whisker surfaces facilitated the interactions between the whiskers and the alumina matrix. Strong bonding was produced at the interface from the interaction, which inevitably resulted in low values of fracture toughness. But the contrary

conclusion was drawn by Homeny et al [63] who used two different categories of SiC whiskers, namely, Silar SC-9 and Tateho SCW-1-S, which had similar properties except for the differences in surface chemistry, to verified the influence of whisker surface chemistry on the fracture toughness of composites. They found that the presence of SiO_xC_y and SiO_2 on the Silar SC-9 whisker surface, compared to only SiC on the Tateho SWC-1-S whisker surface, was a critical factor in allowing the crack wake toughening mechanisms, i.e., whisker pullout and bridging, to operate in the composites fabricated with these whiskers. Using Silar SC-9 as the reinforcement material yielded the higher fracture toughness.

Mechanical behavior

After initial studies of the improvement of SiC_w-Al_2O_3 composite in fracture toughness and strength at room temperature, studies have been extended to other mechanical behaviors of this composite [48].

The creep behavior is one of the key high temperature mechanical properties of SiC_w-Al_2O_3 composite. The first study was done by Chokshi et al [65] who showed that the creep resistance of Al_2O_3 could be improved by two or three orders of magnitude with an addition of 15 vol% SiC_w. This result was further confirmed by more recent studies [74, 65, 75]. Liptski et al [74] found evidence that, at low stress, creep is caused by diffusion and grain boundary sliding facilitated by a glassy phase resulting from the oxidation of the SiC whiskers. As expected for such viscosity-dominated creep, the stress exponent in this stress regime was found to be between

one and two. It may be noted that high-purity monolithic Al_2O_3 at high temperature also exhibits a creep exponent between one and two. In contrast, under high applied stresses, cavitation at the grain boundaries and at the whisker/matrix interfaces dominates the measured bulk deformation. In this creep regime, the stress exponent was found to be between three and eight, depending on temperature and whisker loading. Such high values are typical for tensile creep in ceramics that undergo cavitation. A word of caution should be given, however, with regard to the exact magnitude of the stress exponent since the above results were obtained from flexure tests and the possibility of different creep behavior in tension and compression must be considered. If the material creeps in tension faster than in compression, flexure tests may yield ambiguous results for the creep stress exponent [76, 77].

Morrne et al [64] studied the fatigue behavior under uniaxial cyclic compression by using a through-thickness crack in notched specimens. They found that under these test conditions, the crack growth of the composite is analogous to the crack growth of the monolithic Al_2O_3, but the consistent toughness values represented a 60% increase in toughness compared to unreinforced Al_2O_3. The tension-tension cyclic fracture also showed enhanced resistances [48].

Eykes et al [50] investigated the solid-particle erosion behavior for a series of SiC_w-Al_2O_3 composites with a change in SiC_w volume percent from 0 to 28.8 under typical erosion conditions. Additions of SiC_w to Al_2O_3 provided substantial improvement in erosion

resistance. On the other hand, the erodant particle-size and velocity dependence of the erosion rate decreased as the SiC_w content increased.

The reinforcement is also reported to have a positive effect on properties such as thermal shock. For example, the critical ΔT for quenching into boiling water to induce substantial strength loss was about 250°C and more than 900°C, respectively, for alumina and the composite (20 vol% SiC_w) [70].

The understanding and further development of whisker-reinforced ceramic composites can be advanced by the analysis of the toughness mechanisms and the development of a comprehensive theoretical analysis of the toughening behavior. Current studies indicated that key features in determining which process(s) dominates the toughening process are the whisker strength and diameter, as well as the whisker-matrix interface properties (which are related to the surface chemistry of the whisker) [47, 78].

CHAPTER III

EXPERIMENTAL PROCEDURES

3.1 Fabrication of the Ceramic Matrix Composite

3.1.1 Raw Materials

Commercial Alpha-alumina powder A-16 (donated by Aluminum Company of America) was chosen as the matrix material. The composition of this material supplied by the manufacturer was: Al_2O_3 (99.8 wt%), Na_2O (0.07 wt%), SiO_2 (0.03 wt%), MgO (0.03 wt%), Fe_2O_3 (0.02 wt%), CaO (0.01 wt%), and B_2O_3 (0.001 wt%). Major physical properties of the A-16 were: mean particle size, 0.45 μm; surface area, 8.7 m^2/g; and loose bulk density, 2.18 g/cm^3.

Beta-SiC whiskers (products of former American Matrix Inc., donated by Third Millennium Technologies, Inc.) were used as the reinforcing element coupled into the A-16 polycrystalline Al_2O_3 powders. The characteristics of the whiskers are listed in Table 3.1.

3.1.2 Preparation of Green Samples of CMC

The green samples consisted of 90 vol% Al_2O_3 powders and 10 vol% SiC whiskers.

The SiC whiskers were first ultrasonicated for 30 min. The purpose of this step was to assist the breaking down of whisker agglomerates which seriously inhibits densification and is also the initial failure source. Then Al_2O_3 powders and SiC whiskers were blended together for 2 min in a high speed Branun Grinder. The powder mixture was then pressed uniaxially in a metal die under a

Table 3.1 Characteristics of SiC Whiskers

Characteristic	Physical Property
Crystallographic:	Beta Phase
Purity (%):	99.5
Diameter (μm):	1 - 3 (nominal)
Length (μm):	5 - 60 (nominal)
Bulk density (gm/cm^3):	0.1
Specific Gravity:	3.21
Tensile Strength (GPa):	1.7 - 23.7
Young's Modulus (GPa):	361 - 890

pressure of 230 MPa, which yielded a cylindrical pellet of uniform one-half inch diameter and length ranging from 0.25-0.45 inch.

The resulting green density of the pellet was about 52% of the theoretical density, which was determined by an Archimedes method. The preparation procedure for the green samples is illustrated in Figure 3.1.

3.1.3 Microwave Sintering

Sintering experiments were carried out using an industrial microwave system (Cober, Model S6F) which generated microwave radiation at 2.45 GHz with a maximum output power of 6 kW.

Components of the microwave furnace system

The major components of this microwave furnace system included:

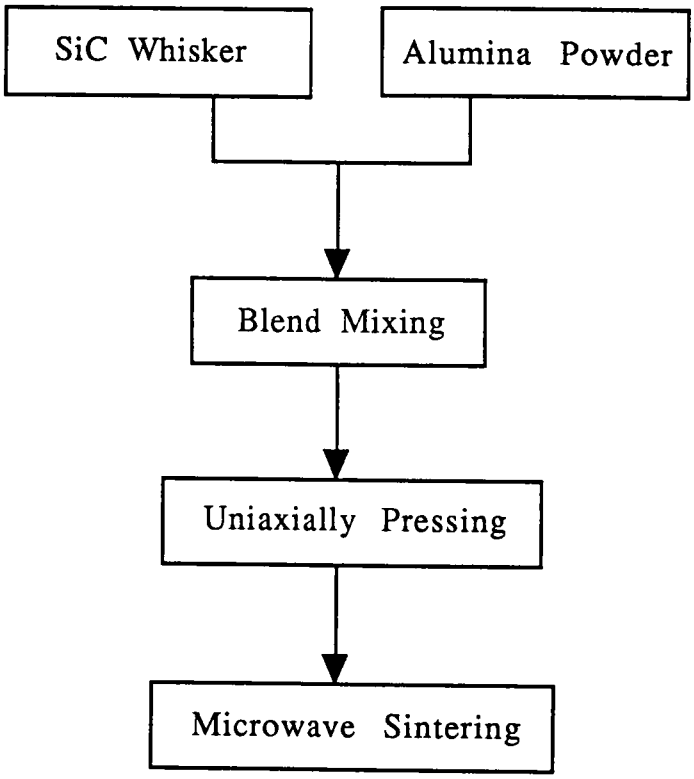

Figure 3.1 Flow chart of preparation procedures of green samples.

(1) microwave generator

The generator is composed of two major parts: (a) magnetron where the microwave power is produced (called forward power), and (b) circulator which is used to protect the magnetron from any reflected power. Both the magnetron and the circulator need continuous water cooling during the operation.

(2) applicator

The applicator is a cavity where the microwave energy is applied from the generator to the loaded samples. A multi-mode resonant cavity was adopted. It was made of stainless steel with an internal dimension of multiples of a half wavelength of the 2.45 GHz microwave frequency. Figure 3.2 is a schematic diagram of the applicator used in this work. The large cavity could be used to sinter large samples but the distribution of the microwave energy was not uniform. The inside small chamber is a reaction cavity which yields more uniform distribution of microwave energy than the large one, and in most cases it is used for high temperature heating. A high temperature insulation board (Babcock and Wilcox 17C) was placed inside the reaction cavity to serve as a thermal shield.

(3) waveguide

The waveguide in a microwave system is a simple interconnection for the transmission of the microwave energy from the source to the applicator. There is a single-stub tuner on the waveguide for matching impedance of the load to the source.

An infrared optical thermometer (Mikron, Model M91H-O) was used for temperature measurement. Figure 3.3 is a block diagram of

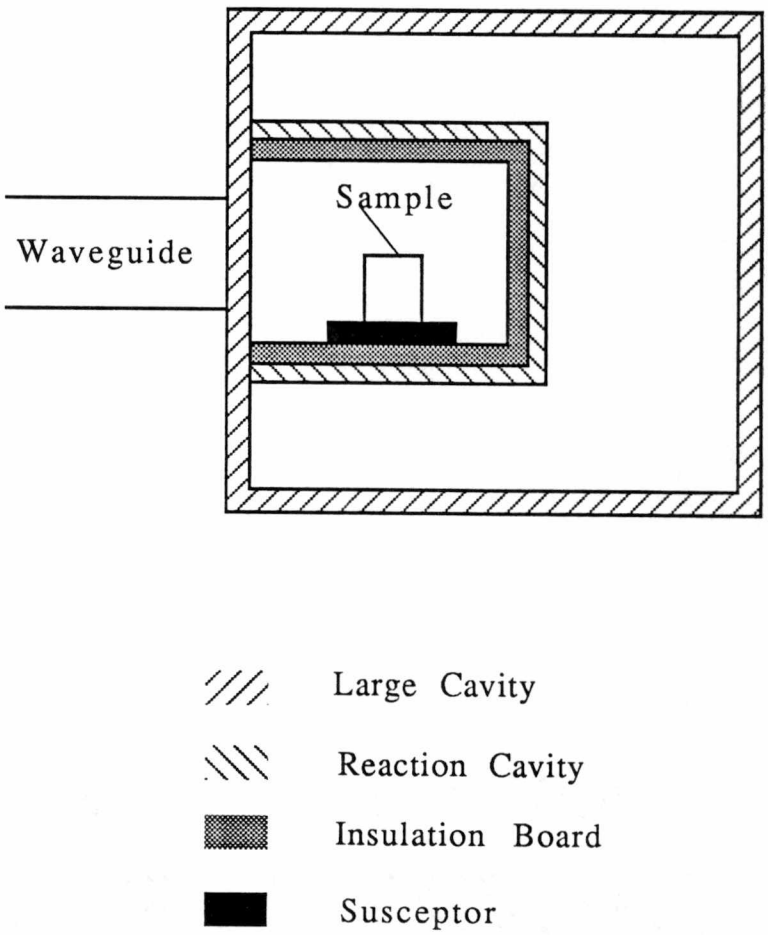

Figure 3.2 Schematic diagram of the microwave applicator.

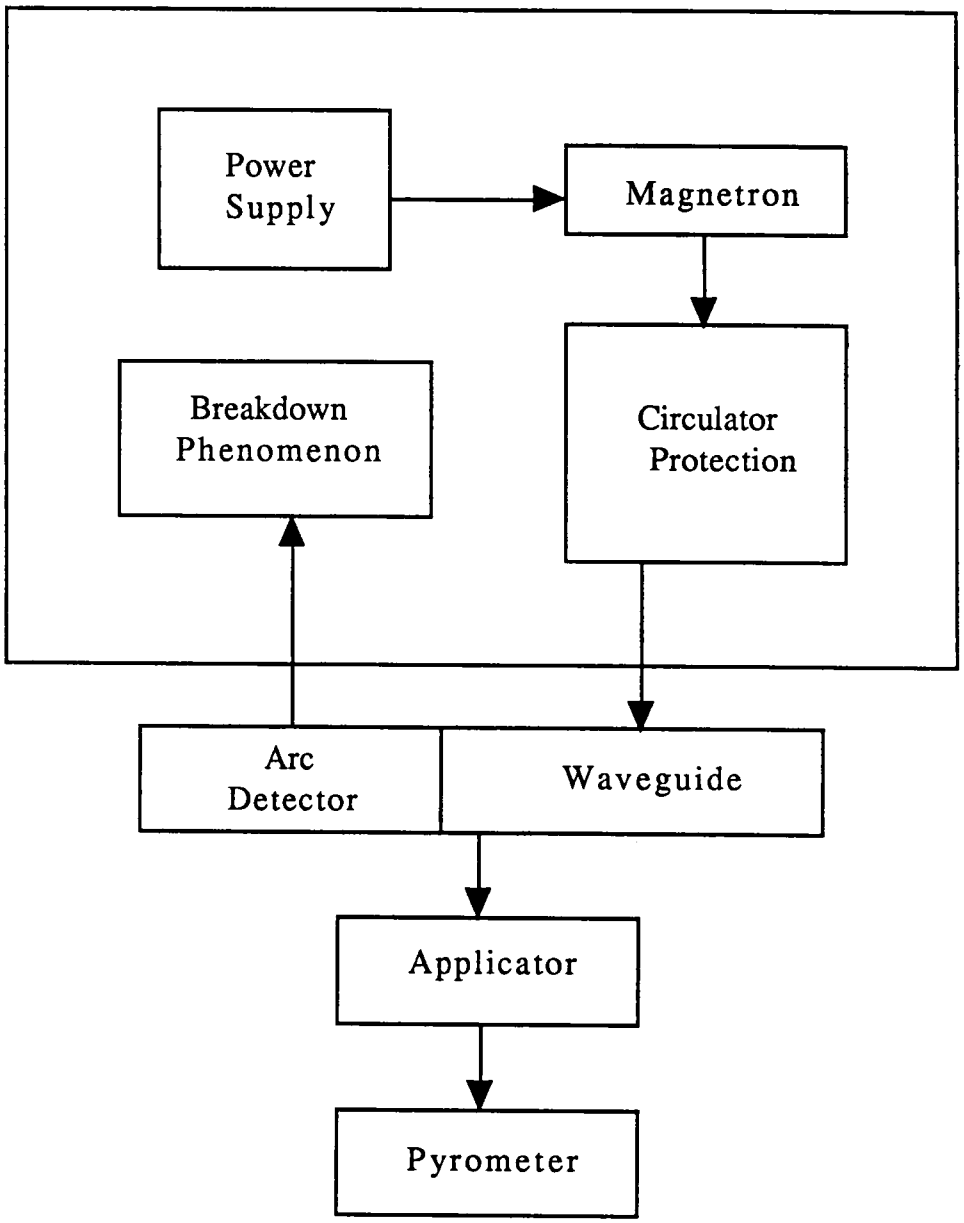

Figure 3.3 Schematic diagram of the mircowave sintering system.

the microwave processing system.

Sintering of CMCs

As mentioned above, Al_2O_3 is a wave transmitting material which has such a low loss-tangent at low temperature that it is very difficult to be directly sintered in a microwave field even with an addition of 10 vol% SiC_w (a high loss-tangent material). A susceptor containing 30 wt% Al_2O_3 and 70 wt% SiC (powders), therefore, was used to improve the sinterability of the composites. In the initial heating step, the heating source came from the susceptor since it easily absorbed microwave energy. Under this condition, the composite gradually changes its dielectric behavior with the increase of surrounding temperature produced by the susceptor. A dramatic increase in the loss tangent of the composite after a certain threshold temperature enables the microwave energy to be a direct driving force for composite sintering.

During the sintering process, the microwave power was controlled by: (1) the increase/decrease of heating/cooling rate as desired, (2) avoiding the phenomenon of thermal run away, and (3) ultimate isothermal sintering temperature. After a certain period of time at the desired sintering temperature, the input power was decreased in a desired rate and was finally turned off at approximate 600°C. The samples were then cooled to ambient temperature inside the furnace cavity.

Two different sintering temperatures, 1550°C and 1650°C, were adopted. At each sintering temperature, three different isothermal processing time intervals were used (10 min, 20 min, and 30 min,

respectively).

Figure 3.4 illustrates typical power and temperature profiles. The heating process can be divided into three progressive stages: namely, preheating, transition, and stable sintering [79]. In the preheating stage, a constant power input rate was applied for the first 20-30 min until the specimens reached the final sintering temperature (in this case, 1650°C). At the end of this stage, the coupling efficiency was so high that thermal runaway would always occur unless careful control of input power was exercised. This was achieved by manual control of the input power, which is the main task of the transition stage where a large decrease of input power was expected. Within 2 min the specimens reached a thermal equilibrium and the final stable sintering stage started with a characteristic of constant input power. The duration of this final stage depended on the desired isothermal sintering time.

3.2 CMC Property Measurements

3.2.1 Density and Porosity Measurements

The density of each sintered sample was carefully measured by an Archimedes method. A detail measuring procedure is referred to ASTM C693-84 [80]. The density of the sample was calculated by the following equation

$$\rho = \frac{W_A \rho_w - W_w \rho_A}{W_A - W_w} \tag{3.1}$$

where ρ is the density of the sintered sample, ρ_w the density of air-free water, ρ_A the density of air, W_A the weight of the sample measured in the air, and W_w the buoyancy force of the sintered

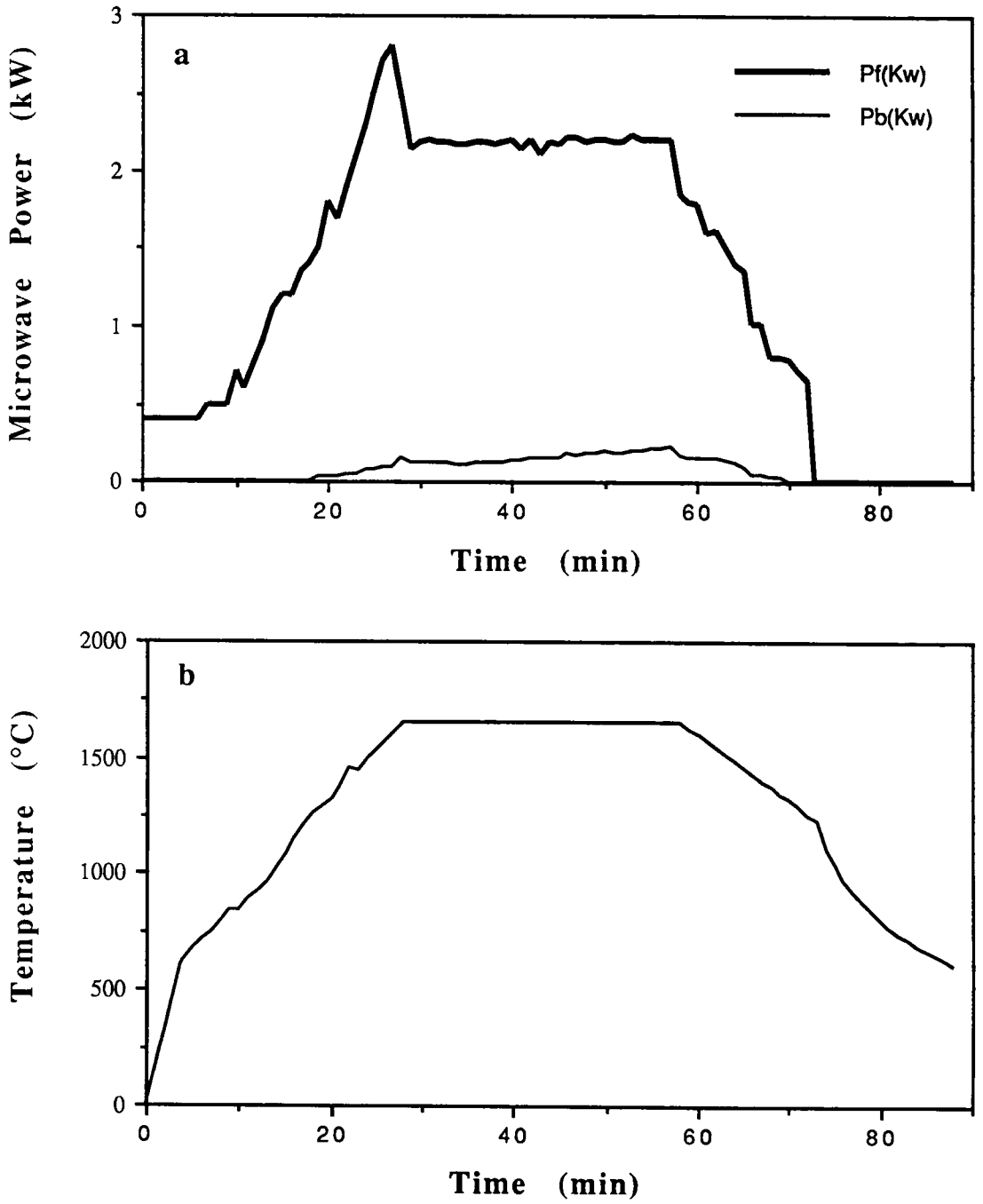

Figure 3.4 (a) Typical power curves in the 2.45 GHz microwave furnace for sintering of Al_2O_3-10 vol% SiC_w CMC at 1650°C for 30 min. Pf is the forward power, Pb is the backward (non-coupled) power, (b) the corresponding temperature profile.

sample in the water.

The total amount of porosity, p, of each sample was calculated by

$$p = 1 - \frac{\rho}{\rho_{th}} \tag{3.2}$$

where ρ_{th} is the theoretical density of the composite material.

3.2.2 Elastic Modulus Measurement

The elastic modulus (E) of a material describes the stress required to deform the atomic bonds per unit strain. Considering the existence of porosity and the random distribution of whiskers in the composite, there is no ideal formula to calculate E better than direct experimental measurement. In this study, the E of the composite was measured by an ultrasonic technique. For a linear, isotropic sample the following relationships exist:

$$E = 2\rho V_S^2(1 + \nu) = \text{Young's modulus} \tag{3.3}$$

$$\nu = \frac{1 - 2\gamma}{2-2\gamma} = \text{poission's ratio} \tag{3.4}$$

$$\gamma = (V_S/V_L)^2 \tag{3.5}$$

where λ is the Lamé constant for isotropic solids, ρ is material density, and V_L and V_S are the ultrasonic wave velocities for compressional waves and shear waves, respectively.

The values of V_L and V_S were determined by the high precision pulse-echo method at a frequency of 5 MHz. The ultrasonic system consisted of a Tektronix 7854 Oscilloscope and a Panametrics Pulse

Receiver 5052PR with a LaB transducer. During the measurements, V_L and V_S were determined for selected samples with five readings averaged per data point.

3.2.3 Hardness Measurements

Hardness of all specimens was measured using a LECO M-400 digital microhardness tester with a Vickers pyramidal diamond indenter. Samples were prepared by using standard ceramographic procedures to produce a mirror surface finish for microstructural observation. The detailed procedures were the following:
(1) grinding the specimens starting with 120 grit SiC paper, then via 220, 320, 600, and 1000 grit SiC papers, (2) polishing the specimens starting with 6 μm and subsequent 3 μm diamond compound on nylon clothing. The final polish was done by using 1 μm diamond compound on silk polishing cloth.

Before hardness testing, ideal loading parameters such as load and loading time had to be determined. It was found that a 500 g load with a 25 second elapse time was the best set of parameters. The machine was calibrated on a standard steel testing block. For each sintering condition, the hardness value was determined from the average value of 10 indentations.

3.2.4 Fracture Toughness Measurements

Fracture toughness determination from indentation method

In general, the traditional method to evaluate the fracture toughness, K_{Ic}, is via a single-edge notch or Cheveron notch bent test. Preparation of the bend test samples for a ceramic material is not as

easy as for a metal sample. In lieu of this traditional materials property evaluation, a surface flaw technique, also called the indentation fracture toughness method, was employed for investigating the fracture properties of the ceramic composites. The advantages of using this technique include not only the simplicity of the specimen preparation but also the smaller specimen dimension, which was very suitable for the microwave sintered pellets. The flaw (crack) can be induced by a Vickers indentation (Figure 3.5). The toughness is then determined from the fracture load P and the flaw size as measured on the specimen surface. A number of equations have been proposed in the past [81-87]. The most widely used equation to evaluate the fracture toughness, however, is as follows [83]:

$$K_{Ic} = (0.016 \pm 0.004)\,(E/H)^{1/2}(P/c^{3/2}) \qquad (3.6)$$

where (0.016 ± 0.004) is a "calibration constant" which is obtained by averaging over a broad spectrum of materials, H is the Vickers hardness, E is the Young's modulus of the sample, P is the indented loading, and c is the half crack length on the specimen surface, which is induced by the load P.

Eqn. (3.6) yields significantly lower values for the fracture toughness of various alumina samples than these obtained from conventional methods of measurement. This can be seen in Figure 3.6 which is reproduced from the work of Antis et al [83]. Based on their studies, a corrected calibration constant with a value of 0.023 was determined for alumina. Eqn. (3.7) is the modified version of Eqn.

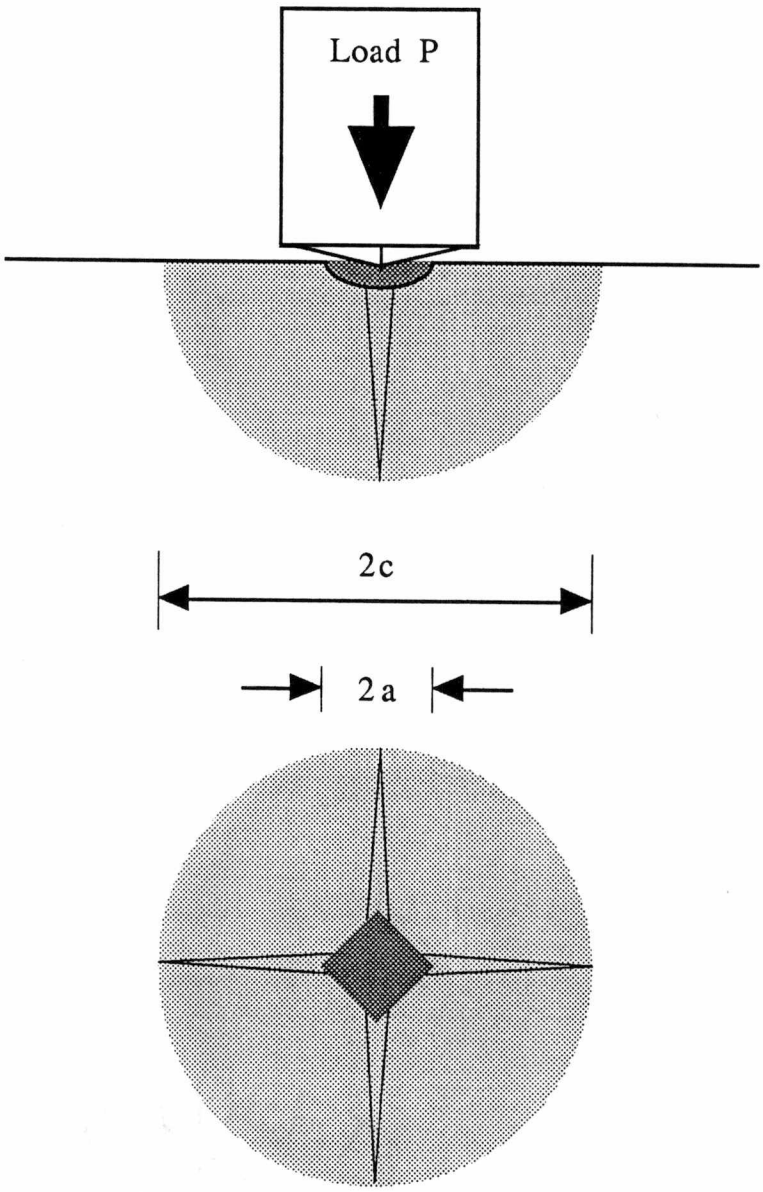

Figure. 3.5 Schematic diagram of the flaw pattern by Vickers indentation.

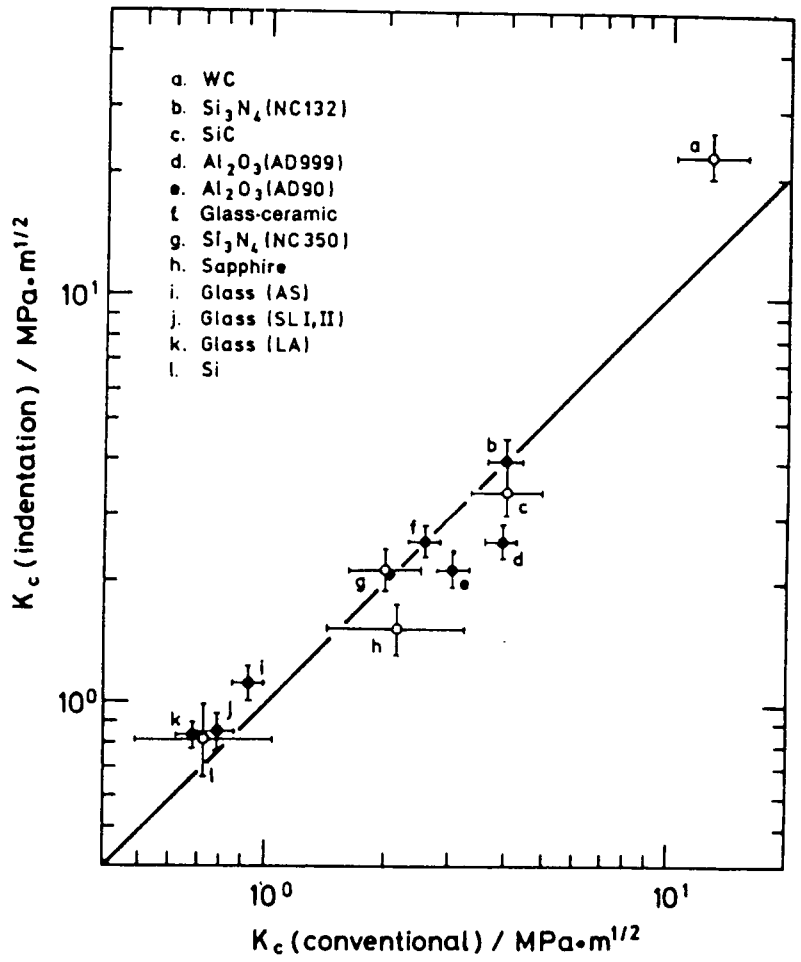

Figure 3.6 Plot demonstrating the correlation between toughness values determined by indentation and by conventional means.

(3.6) and was to be used in this study for the calculation of K_{Ic} from direct crack length measurements:

$$K_{Ic}= 0.023\ (E/H)^{1/2}(P/c^{3/2}) \qquad (3.7)$$

The following criteria should be satisfied in order for Eqn. (3.7) to be valid:

(1) any prospective test specimen must produce a well-defined radial crack system (a well-defined radial crack could be found when the indentation fracture parameter ($P/c^{3/2}$) of the specimen was independent of load P),

(2) the crack length seen on a polished surface must be as long or longer than the diagonal length of the indentation, i.e., $c \geq 2a$, and

(3) there must be no chipping or lateral cracking.

In order to obtain accurate testing results, it is essential that the testing surface should contain no pre-existing stresses prior to indentation; the fracture parameter $P/c^{3/2}$, otherwise, would be affected due to the presence of the stress. A well-controlled indentation test offers the prospect of highly reproducible deformation-fracture geometry, together with simplicity and economy in data gathering.

Specimen preparation

The preparation of specimens was similar to the preparation of specimens for the hardness tests. The only difference was that a 0.25 μm diamond compound was used as the final polishing step. These progressive polishing procedures eliminated residual stresses by polishing out the plastic zone and an optical surface was then

produced so that the crack size could be accurately determined.

Testing

The Vickers indentations were made by using a Tukon Microhardness tester unit. Each sample was indented by different loads (P) ranging from 4 kg to 10 kg over which the indentation patterns remained well defined: at the lower end by the minimum requirement $c \geq 2a$ for validity of Eqn. (3.7); at the upper end by avoiding chipping. For each different load P, an average value from five indentations was used to determine the mean crack length c. In order to obtain more accurate measurements, the crack length c was measured using a LECO M-400 digital microhardness tester unit immediately following the microhardness test.

3.3 Characterizations of CMSs

Structure characterizations were performed using transmission electron microscopy (TEM) and scanning electron microscopy (SEM). Chemical composition analyses were conducted using X-ray photoelectron spectroscopy (XPS) and energy-dispersive X-ray spectroscopy (EDS). Phase analysis was carried out using X-ray diffraction (XRD).

The TEMs used in this study included a 200 kV Hitachi HF2000 field emission TEM, a 200 kV Hitachi H800 scanning transmission electron microscope (STEM) equipped with a LaB_6 electron source and a Link X-ray detector, and a 100 kV Hitachi H600 TEM. The SEM used was a Hitachi S800 field emission SEM attached with a Link X-ray detector. The XPS was performed with a Perkin-Elmer PHI 5100

ESCA system. A Rigaku X-ray diffractometer was employed for phase identification.

3.3.1 Raw materials

As-recieved Al_2O_3 powders and SiC whiskers were characterized by TEM and SEM to determine particle size distribution, surface morphology, defect structures, and crystallography. The surface chemistry of the SiC whiskers was analyzed by XPS.

Structure analysis of SiC_w

Whisker specimens were prepared for TEM analysis either by direct dispersion onto a holy carbon support film (for characterization of surface and defect structures) or by ultramicrotomed thin-sliced whiskers embedded in epoxy (for high resolution imaging of whisker microstructure). The defect structures were studied by both bright field and dark field imaging methods. The whisker crystal orientation was studied by the selected area diffraction method.

Surface chemistry analysis of SiC_w

Bulk whisker surface chemistry analysis was accomplished using a X-ray photoelectron spectrometer. At first, a broad-energy low-resolution "survey scan" was taken to determine where peaks were located then followed by narrow width high-resolution scans around the peaks observed in the survey scan. Calibration of the energy scale was accomplished by using the standard SiC signal [88].

3.3.2 Sintered CMCs

Interfacial structure analysis

The structures of interfaces between Al_2O_3 grains and SiC whiskers were examined in by TEM. Both bright field (BF) and dark field (DF) imaging methods were used. Conventional selected area diffraction (SAD) and convergent beam electron diffraction (CBED) techniques were employed to observe the whisker and alumina grain orientations while adjusting their orientations with a tilting stage. Interfacial composition was examined using EDS with an electron probe size of the order of 80 Å.

TEM thin foils were prepared by one of the following methods:
(1) Specimens were prepared by sectioning a disk from the center of each sintered cylindrical pellet sample with a direction normal to the cold pressing axis. Disks were ground, polished, and dimple-polished prior to ion milling. Finally they were ion milled using the Gatan ion beam thinner at a voltage of 6 kV and incidence beam angle of 15° until the specimen was perforated.
(2) The composites were embedded in epoxy, then thin-sliced by ultramicrotome using a diamond knife.

Fractography study

Samples from each sintering condition were selected to undergo fractography study using SEM. Compression tests were used to created the fracture surface. The fractured surface was coated with a thin film of gold (50 Å) to avoid electron beam charging.

X-ray diffraction analysis of CMCs

X-ray diffraction analysis using a rotating anode diffractomer and monochromated CuK_α radiation was used to determine the phases present in the composite. In a typical diffraction analysis set-up (tube voltage 35 kV, tube current 30 mA, scan rate 0.5°/min, Ni filter), the X-ray beam was directed onto a sample surface which formed an angle theta (θ) with respect to the incident X-ray beam. A detector was placed symmetrically, also at an angle θ to the sample surface (2θ to the X-ray beam), to receive the diffracted X-rays. Finally, the diffraction pattern was recorded in the form of 2θ vs. I (X-ray intensity). The scanned 2θ ranged from 20° to 140°.

After the experiment, values of d ($d = \lambda/\sin 2\theta$) and I/I_{max} (I_{max}, the maximum X-ray intensity recorded) were tabulated, JCPDS (Joint Committee on Powder Diffraction Standards) was used to identify the unknown pattern through a computer searching program.

CHAPTER IV

RESULTS AND DISCUSSION

4.1 Raw Materials

4.1.1 Al_2O_3 Powders

SEM analysis indicated that there existed quite a large particle-size distribution in the Al_2O_3 powder (Figure 4.1). The largest particle was more than twice the mean particle size. Clusters of agglomeration were randomly found within the powders.

4.1.2 Morphologies and Surface Chemistry Analysis of SiC Whiskers

The general morphology of the whiskers is shown in Figure 4.2. The SEM micrographs revealed that the whiskers exhibited a large variety of morphology. The typical irregularly shaped whiskers are shown in Figure 4.3. Because of the irregular shape, the whisker surface was rough on a sub-micrometer scale, and the whisker surface area was significantly increased along with the corresponding interfacial area for bonding to a fine-grained ceramic host matrix. TEM study indicated that the whiskers were combinations of heavy defected β-phase SiC (3C).

In the TEM imaging analysis, most of the whiskers exhibited stacking faults on the (111) planes which are normal to the whisker axis (Figure 4.4), spaced 2 to 20 nm apart. Electron diffraction analysis of cross-section specimens indicated that the major whisker facets were parallel to the {111} planes. A thin amorphous layer (the thickness ranged from 2 to 200 nm) was found surrounding the

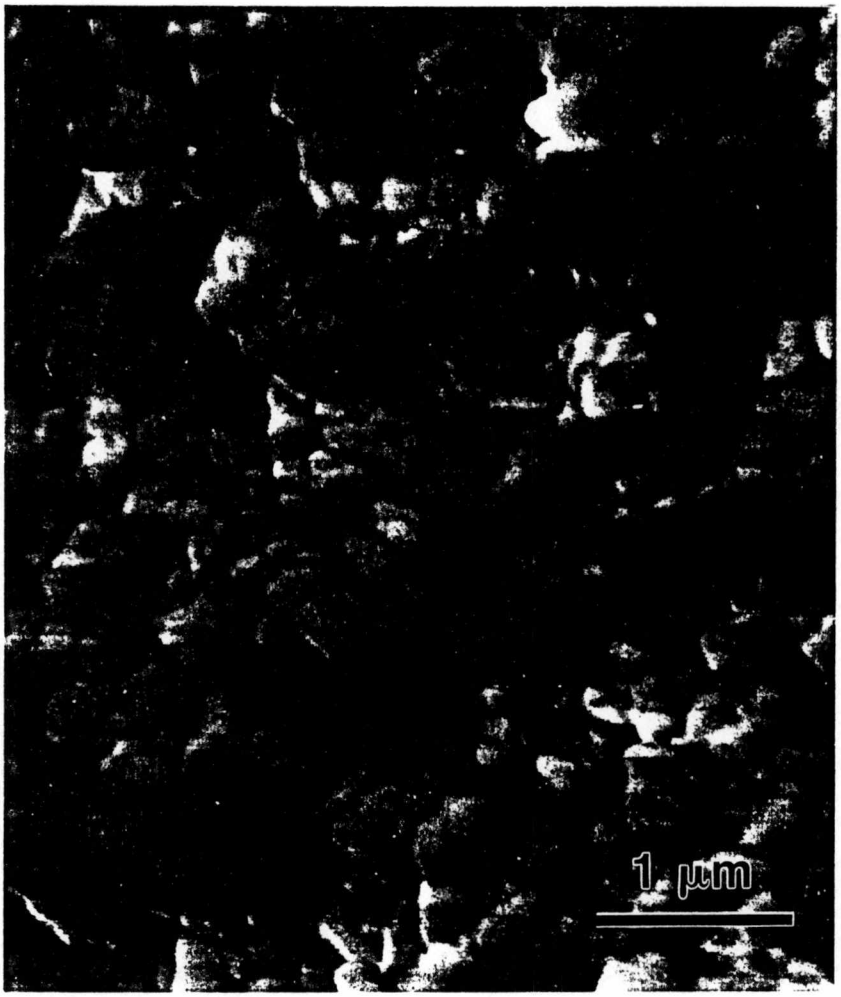

Figure 4.1 SEM micrograph of AG-16 Al_2O_3 powders used as the matrix material.

Figure 4.2 General morphology of SiC whiskers used as the reinforcement material.

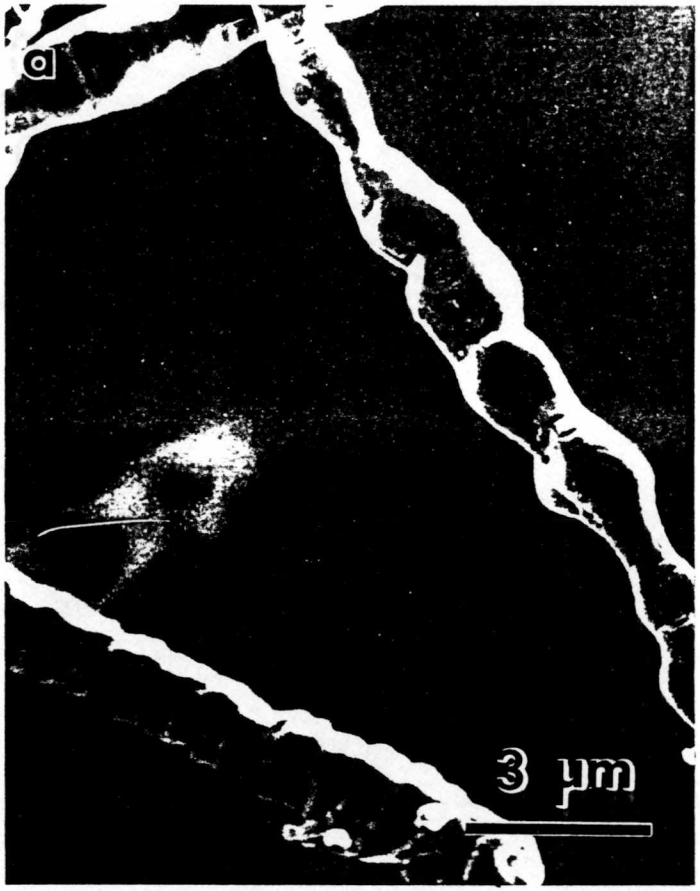

Figure 4.3 Typical irregular shaped whiskers:

(a) nobbled,

(b) microfaceted, and

(c) pine cone shaped.

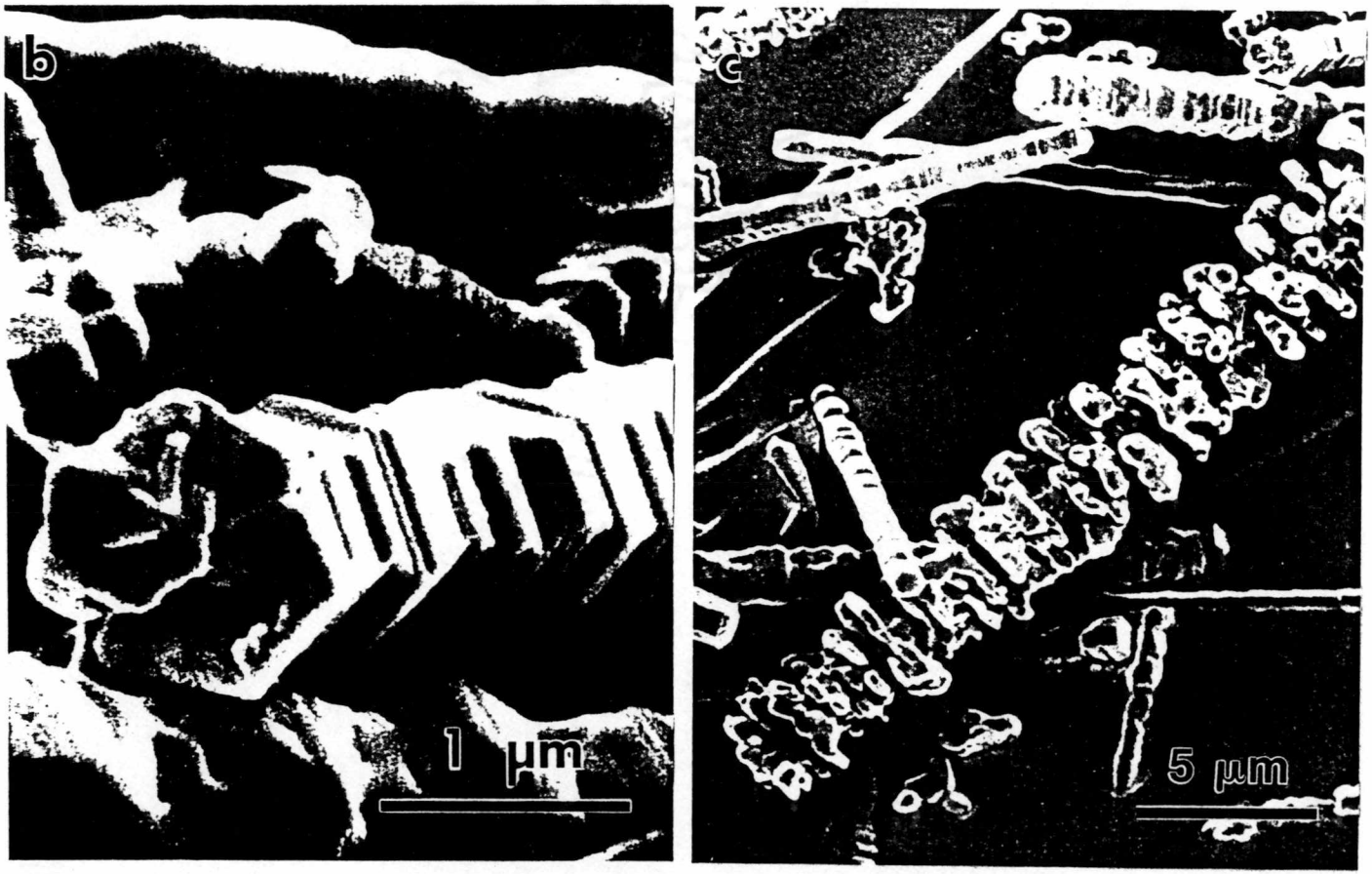

Figure 4.3 continued

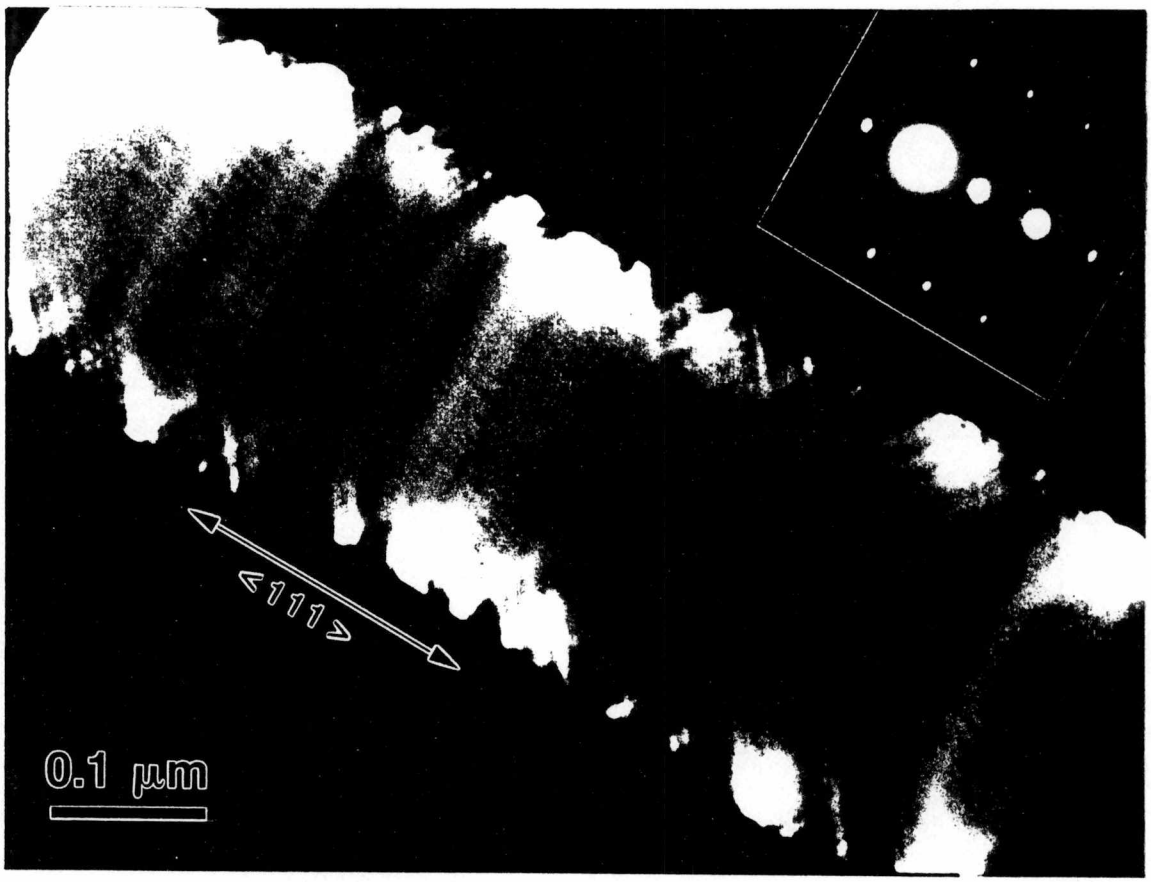

Figure 4.4 Stacking faults on {111} plane of the whisker. The inset shows the selected area diffraction pattern.

whiskers (Figure 4.5).

The major elemental composition on the whisker surfaces was observed to be composed of silicon, carbon, and oxygen (see Figure 4.6) in the atomic ratios 100:118:188. The silicon 2p photoionization signal showed Si-C and Si-O components in the ratio 38.54:61.46 (Figure 4.7). The binding energy of the Si 2p(1) peak was 103.06 eV, which suggested the presence of a SiO_2 layer [89].

In Figure 4.7, the smoothed spectrum was synthesized using a Gauss function curve fitting routine to aid in determining the composite peak binding energy. Table 4.1 lists the atomic fraction vs. various binding energies of different XPS peaks of silicon, carbon, and oxygen on the surfaces of the whiskers.

Table 4.1 SiC Whisker Surface Atomic Fraction (at%) vs. Binding Energy (BE)

		at %	BE (eV)
Si	peak 1	9.5	100.40
	peak 2	14.91	103.06
C	peak 1	8.00	282.47
	peak 2	20.90	284.99
O		45.89	532.1

4.2 CMC Properties

4.2.1 Density and Porosity

Table 4.2 lists the densities and the porosities of the various

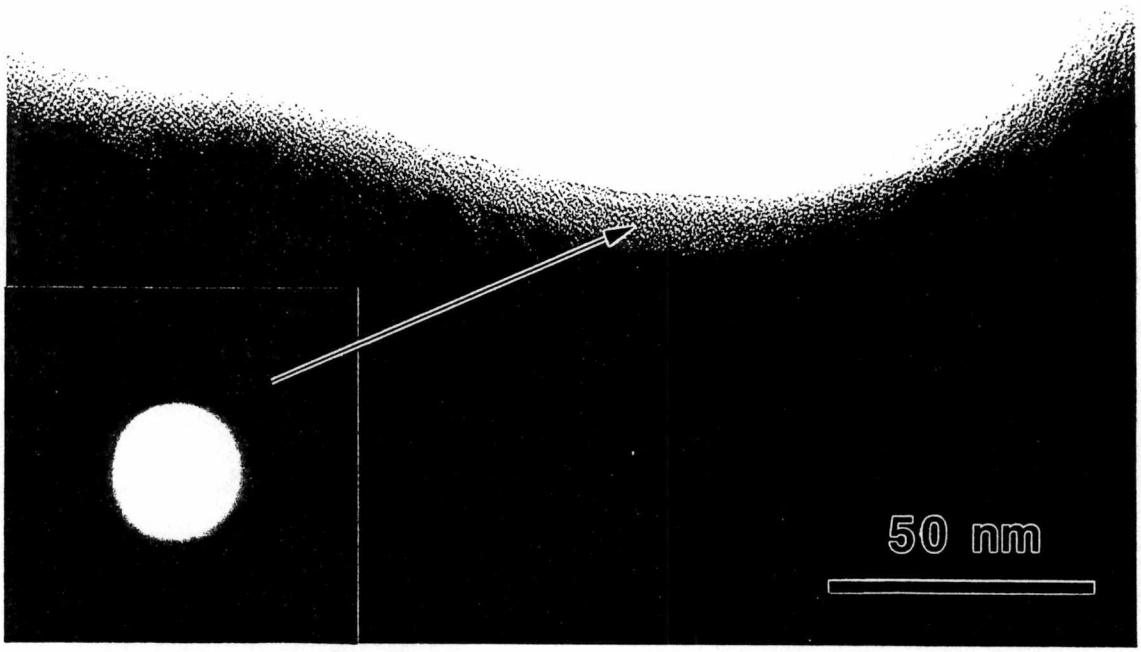

Figure 4.5 Amorphous layer on the surface of the whisker. The inset shows the microdiffraction pattern of the amorphous layer.

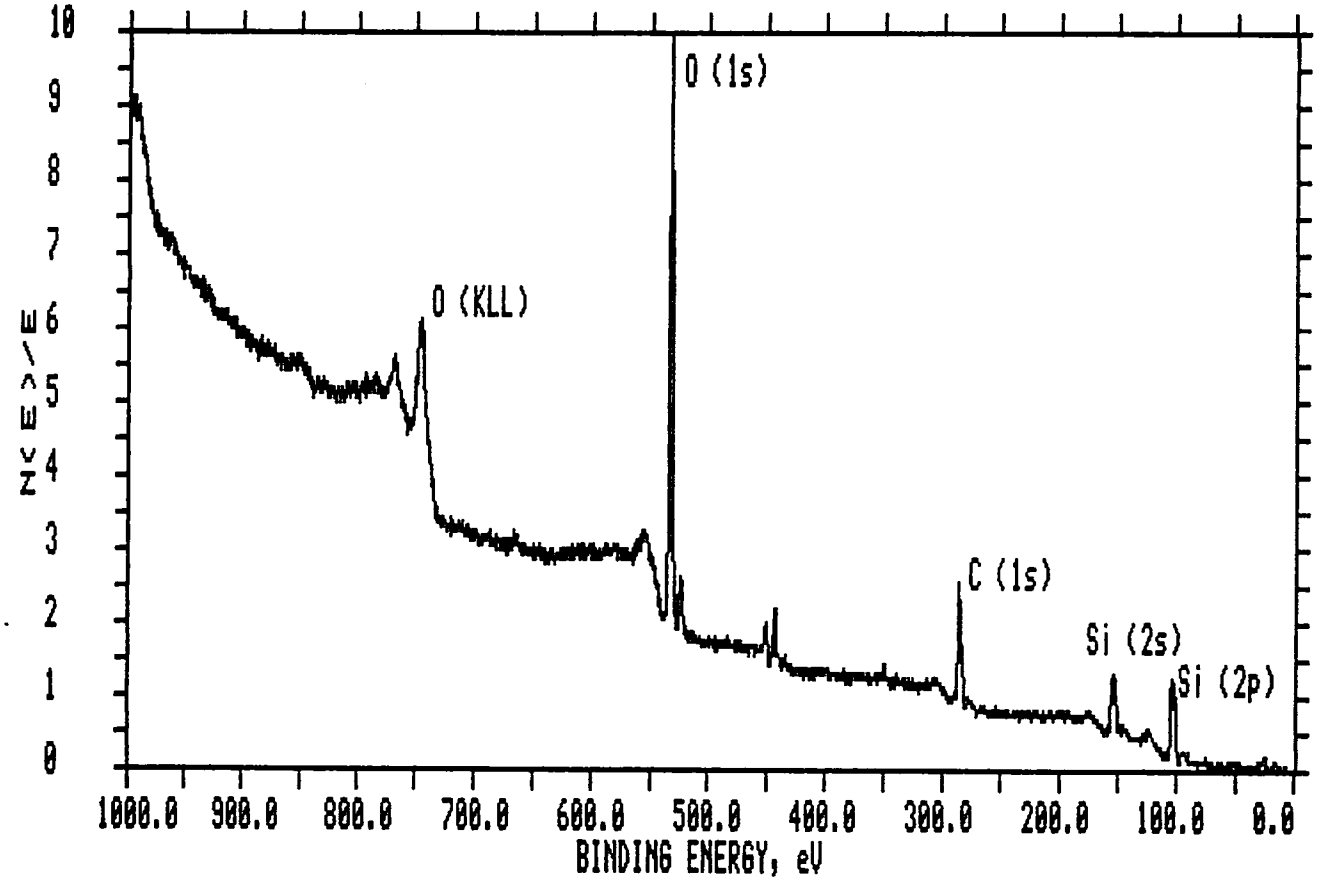

Figure 4.6 The survey spectrum XPS analysis of the as-received SiC whisker surface.

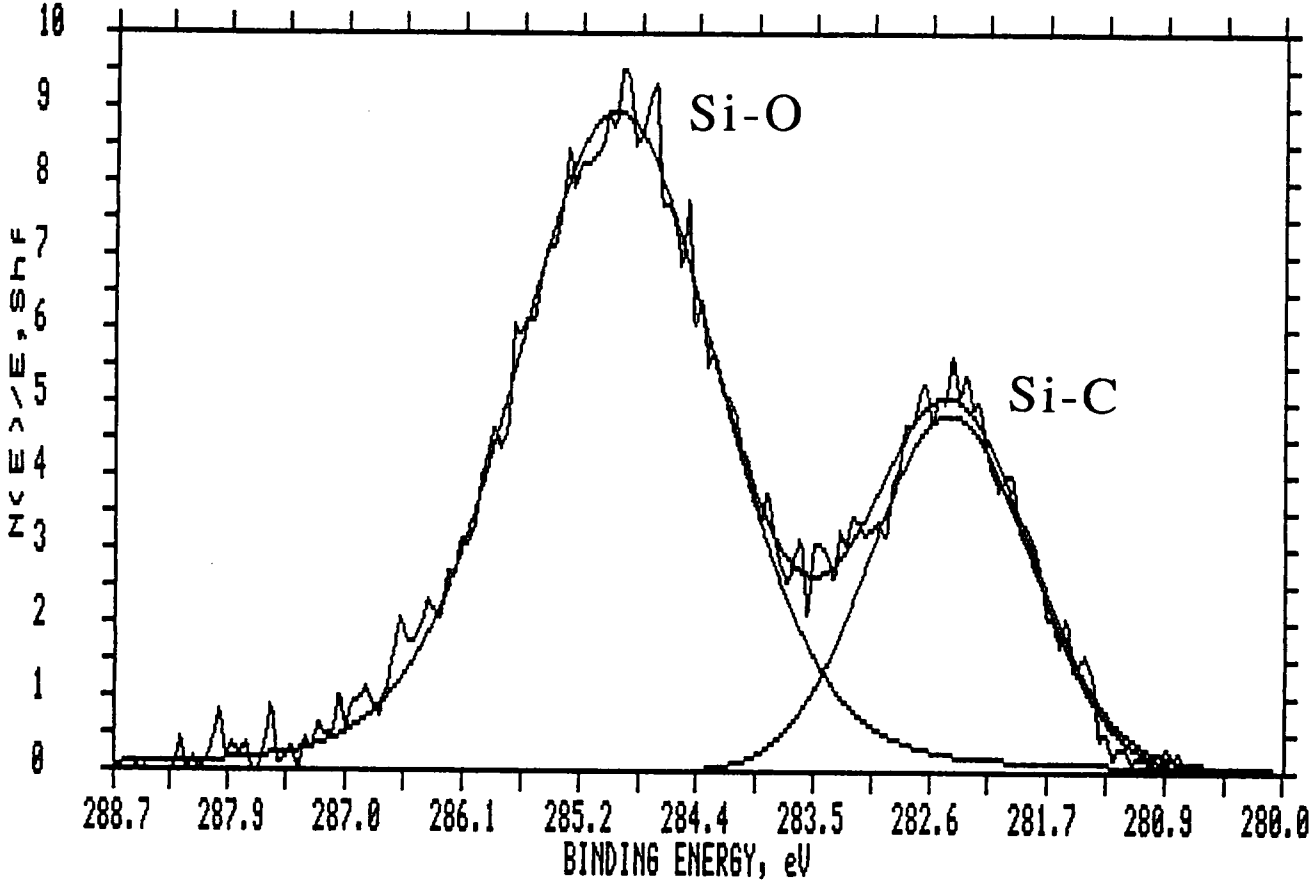

Figure 4.7 Silicon 2p spectrum of the surface of the as-received SiC whisker surface.

Table 4.2 Density and Porosity of the Composite

Sample Group	Sintering Parameter Temp (°C)/Time* (min)	Density ρ (g/cm^3)	Total Porosity p ($p = 1- \rho/\rho_{th}$#) (%)
9	1650/10	3.78	3.0
10	1650/20	3.87	0.8
13	1650/30	3.80	2.6
11	1550/10	3.88	0.5
12	1550/20	3.88	0.5
14	1550/30	3.88	0.5

*isothermal sintering time at peak temperature;
#ρ_{th} = 3.90 g/cm^3.

composites under different processing conditions. The densities were varied from 96.8% to 99.5% with different sintering parameters, suggesting that satisfactory densification can be created by microwave processing. It is believed that the high and rapid densification rate of the microwave sintering was achieved by the microwave internal volume heating mechanism. Proposed explanations are that (1) enhanced transport properties/activation energy occurs in an electromagnetic field [90, 19], (2) activation of grain boundary and lattice diffusion are the major driving forces in the microwave sintering [79], or (3) the melting temperature in the grain boundary is lower than that of the bulk material itself, which helps mass rearrangement and hence high density [16].

4.2.2 Young's Modulus and Hardness

The mechanical properties of ceramics are strongly dependent on grain boundary structure and composition, particularly when the composite materials originate from fine-grained powders that have been sintered [91].

The Young's modulus measurement in this study revealed significantly lower values in comparison to the reported data for conventionally sintered composites. The measured Young's modulus ranged from 182 to 282 GPa, while the reported data for conventionally sintered samples is on the order of 400 GPa [92]. All measured values of E and H_V for the composite are listed in Table 4.3.

It was observed that after microwave sintering, Al_2O_3 grains were separated by a thin amorphous layer (Figure 4.8). The existence

Table 4.3 Hardness and Young's Modulus of the Composite

Sample Group	Sintering Parameters Temp (°C)/Time* (min)	Hardness Hv (GPa)	Young's Modulus E (GPa)	E_0 of Full Desity (GPa)
9	1650/10	9.94	257.1	282.38
10	1650/20	9.40	245.6	249.60
13	1650/30	10.39	282.3	294.76
11	1550/10	7.45	182.3	184.66
12	1550/20	8.62	195.6	198.63
14	1550/30	8.09	189.8	191.07

*isothermal sintering time at peak temperature.

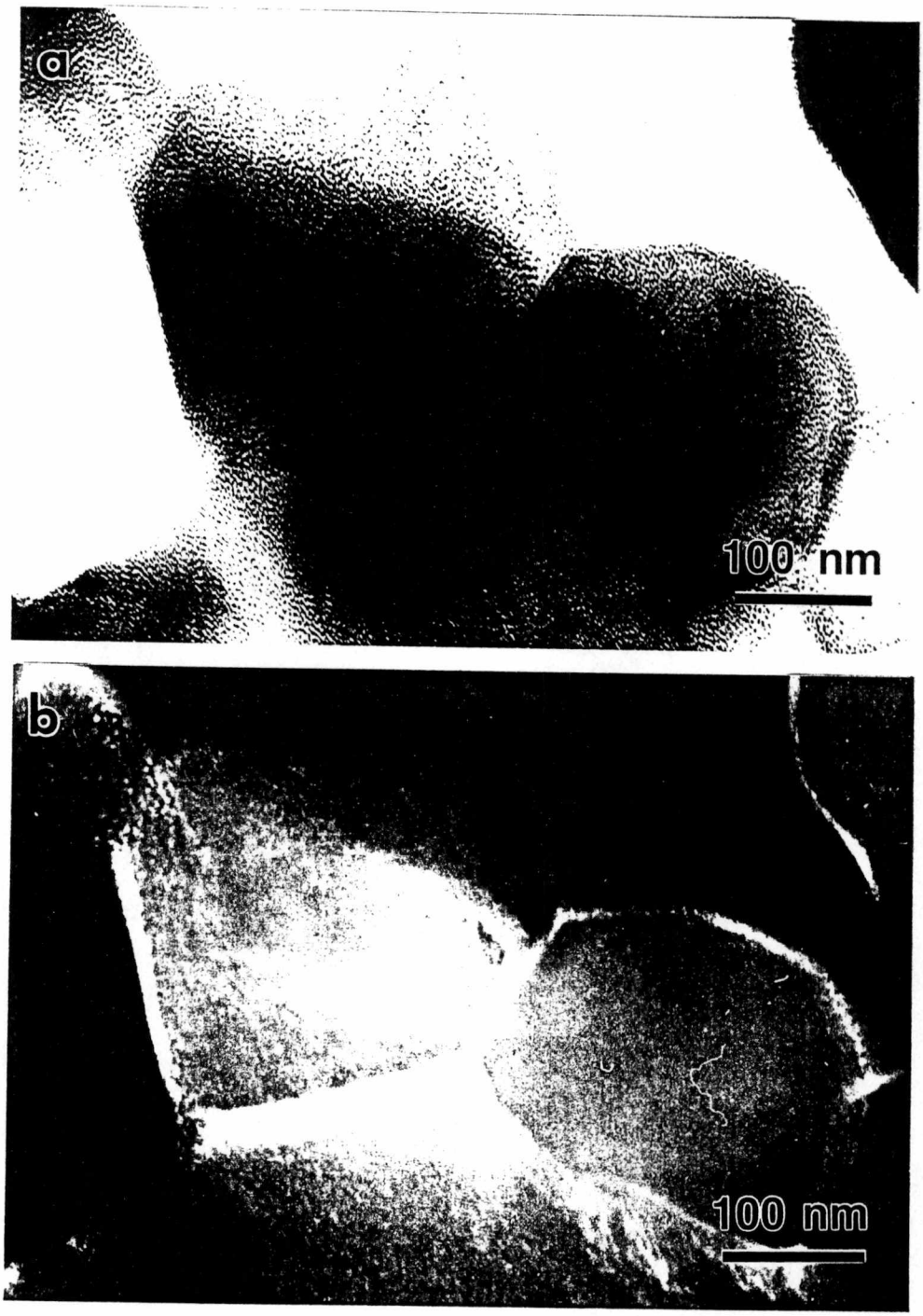

Figure 4.8 (a) TEM bright field image of the Al_2O_3 grains of the CMC sintered at 1650°C for 20 min, (b) corresponding TEM dark field image showing amorphous layers surrounding the Al_2O_3 grains.

of the amorphous layer may create weak bonding in the grain boundary region; and some microcracking may occur along the boundary due to thermal expansion coefficient mismatch during cooling or after suffering local stress, which results in a decrease of the hardness of the composite.

Since the whiskers were randomly oriented in the matrix, the elastic behavior of individual whiskers can be presumed to be similar to that of grains in the polycrystalline SiC, in which the orientation dependent contributions of individual grains balance each other and the experiment error is minimized during measuring. From the measured E of the composite, the Young's modulus of the fully dense material, E_0, can be calculated from Mackenzie's equation [93]:

$$E = E_0(1 - 1.9p - p^2) \qquad (4.1)$$

where p is the porosity of the composite.

The causes for the low values of Young's modulus is not very well understood due to limited numbers of experiments. One possibility still could be related to microcracking on the grain boundary, which decreases the ultrasonic wave velocities for compressional waves and shear waves. The atomic bonding change by the electromagnetic radiation could be another possibility.

4.2.3 Fracture Toughness

Within the loading range, the occurrence of indentation which was judged unacceptable, i.e., chipping or lateral cracking, was infrequent. One example of such an unacceptable indentation is shown in Figure 4.9.

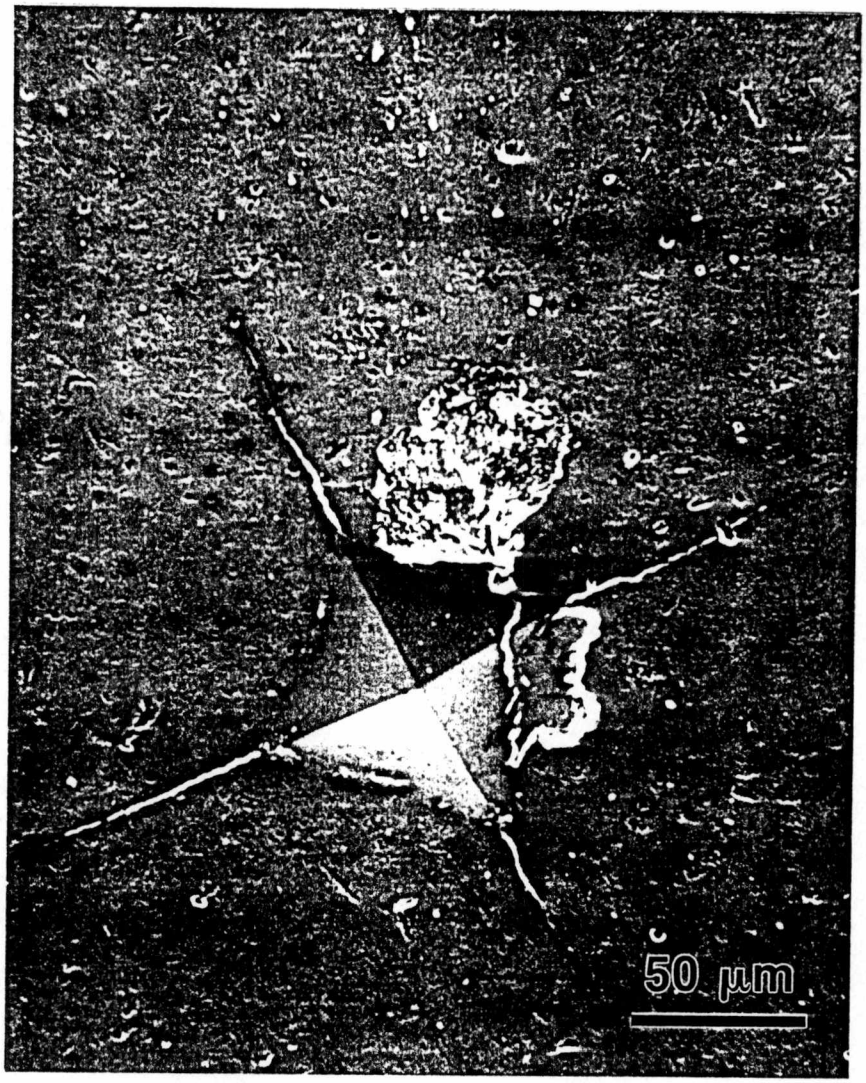

Figure 4.9 Occasionally, lateral cracks occurred in some of the indentation, which is unacceptable for toughness measurement.

The plot of the fracture parameter ($P/c^{3/2}$) vs. working range of load P from the indentation test indicated that the crack profiles belonged to the radial crack response (Figure 4.10). The fluctuation was relatively small, only 10% at the worst case over the average value, which meant that the fracture parameter $P/c^{3/2}$ was quite insensitive to the load P. It was determined that Antins' equation could be adopted to calculate the fracture toughness, K_{Ic}, of the composite. The average fracture parameter was calculated as follows:

$$\text{Average Fracture Parameter} = \frac{\sum_{i=1}^{n} \frac{P_i}{\left(\sum_{j=1}^{m} c_{ij}\right) / m}}{n} \qquad (4.2)$$

where n is the total number of different loads, i indicates a certain load, P_i is the ith load, m the total number of indentations at each load, j indicates a certain indentation number, and c_{ij} the crack length of the jth indentation corresponding to ith load P_i.

The fracture toughness of the composite measured by this indentation method is listed in Table 4.4. The fracture toughness of microwave sintered SiC_w-Al_2O_3 CMCs (K_{Ic} = 4.5 to 5.3 MPa$\sqrt{m}$) was about 80 to 110% higher than that of hot-press sintered monolithic alumina (K_{Ic} = 2.5 MPa$\sqrt{m}$, grain size 1-2 nm) [46]. The fracture toughness data of microwave sintered monolithic alumina is not available at this time. The interpretation of the results will be discussed in a later section. The presence of a thick SiO_2 layer on the whisker surface would reduce the fracture toughness of the

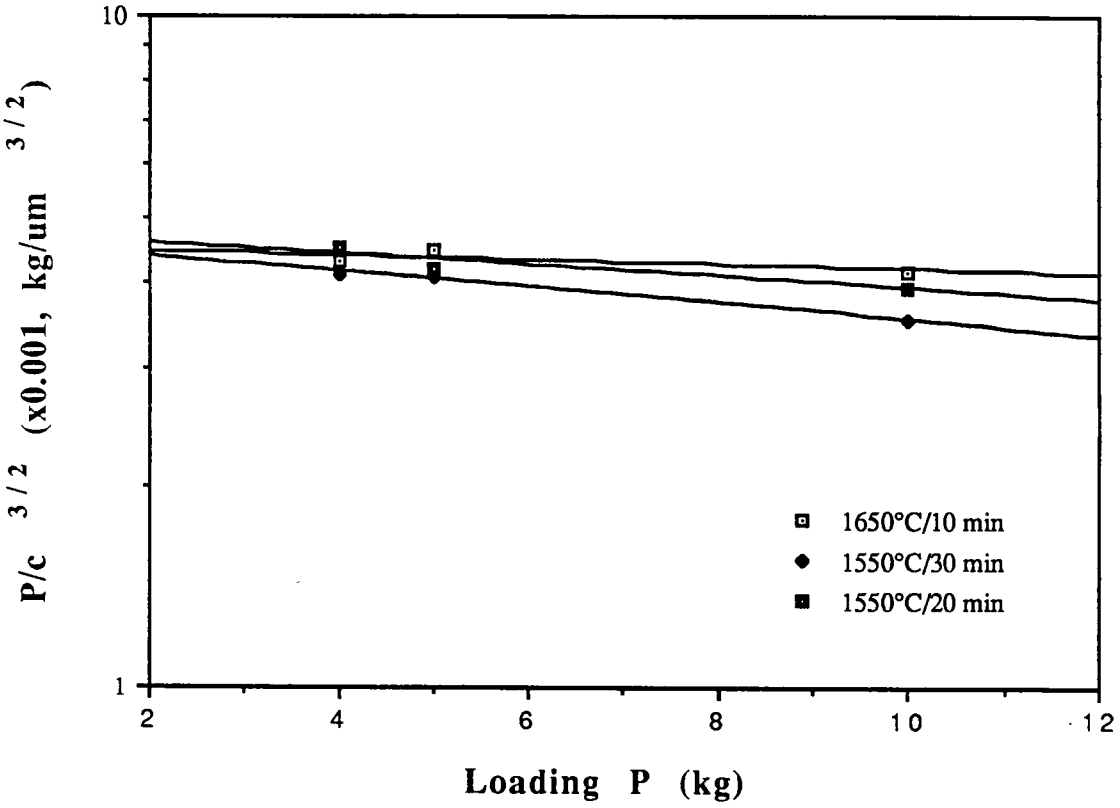

Figure 4.10 Examples of plot of $P/c_0^{3/2}$ over working range of load P for tested CMCs for which well-defined radial cracks could be obtained.

Table 4.4 Fracture Toughness Measured by Indentation Method

Sample Group	Sintering Parameters Temp (°C)/ Time (min)	Fracture Toughness K_{Ic} (GPa)
9	1650/10	5.0
10	1650/20	5.3
13	1650/30	5.2
11	1550/10	4.5
12	1550/20	4.7
14	1550/30	4.6

composite [89]. It is expected that using etch-cleaned whiskers would further increase the values of fracture toughness.

4.3 CMC Structures and Phases

Figure 4.11 shows the typical structure of the composite. SiC whiskers were uniformly distributed in the matrix. Most of the whiskers had a length in the range from 10 to 60 μm which was within the range of the aspect ratio provided by the manufacture. Some of the whiskers might have suffered breakage during mechanical blending. In the high magnification micrographs of TEM, the serrated surface of the whisker appeared to have good bonding with the matrix through an amorphous layer (Figure 4.12). Dark-field studies also indicated the presence of a thin (< 7 nm thickness) amorphous layer on a large portion of Al_2O_3 grain boundaries (Figure 4.13). The melting temperature of Al_2O_3 is 2045°C which is about

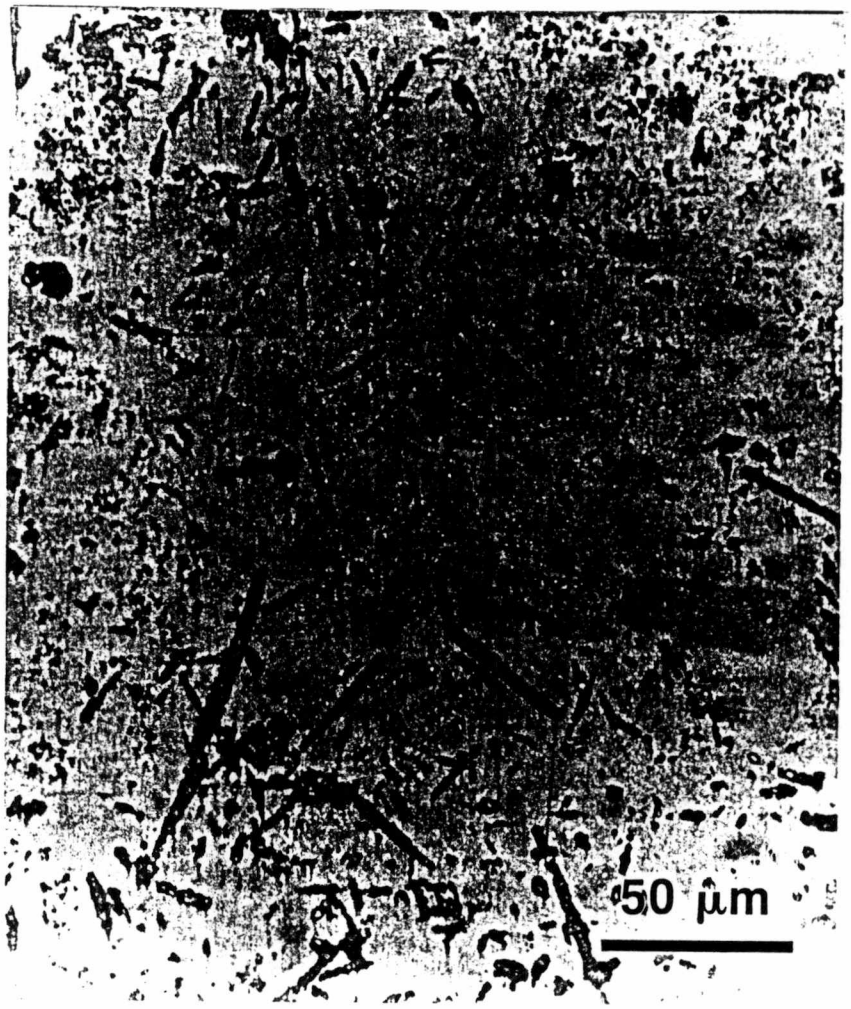

Figure 4.11 Optical micrograph of a typical structure of Al_2O_3-10 vol% SiC_w composite.

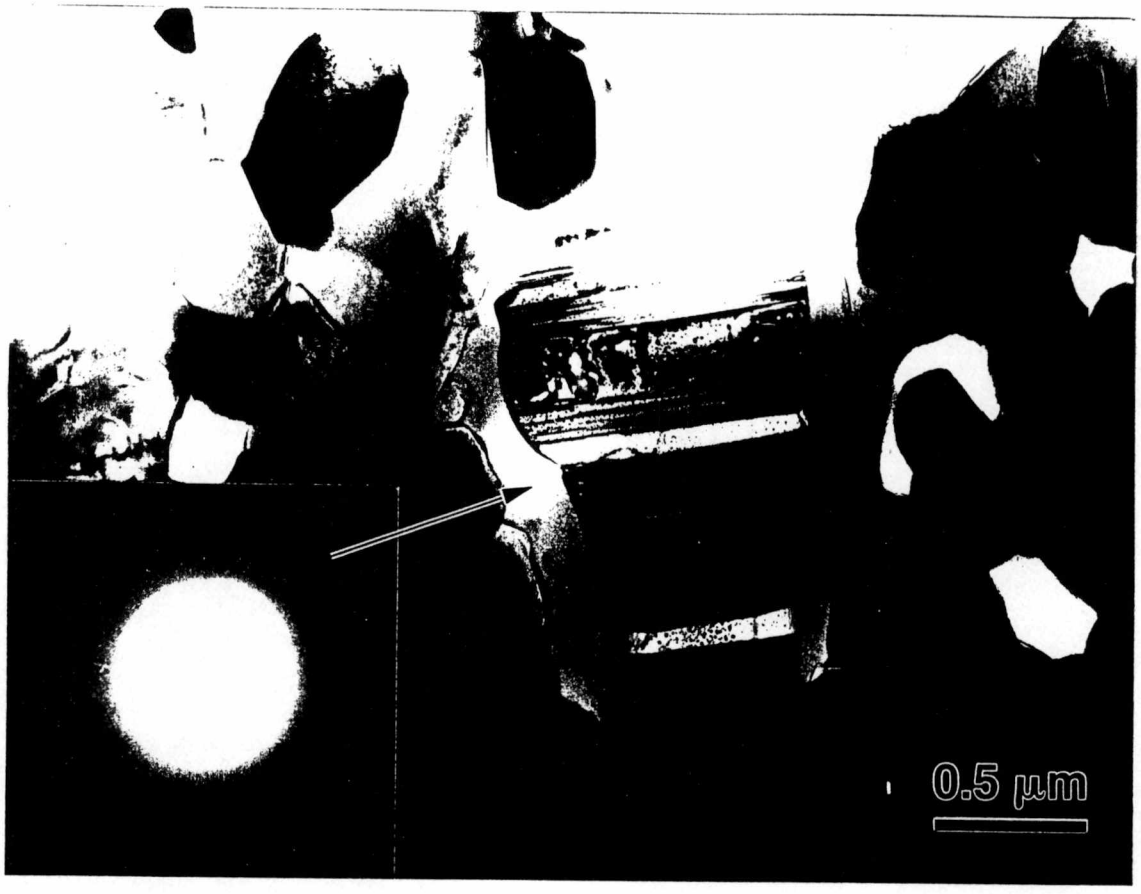

Figure 4.12 TEM bright field image of a SiC whisker bonded with the alumina matrix through an amorphous interphase. The inset shows the selected area diffraction pattern of the interphase region with a typical amorphous diffraction feature.

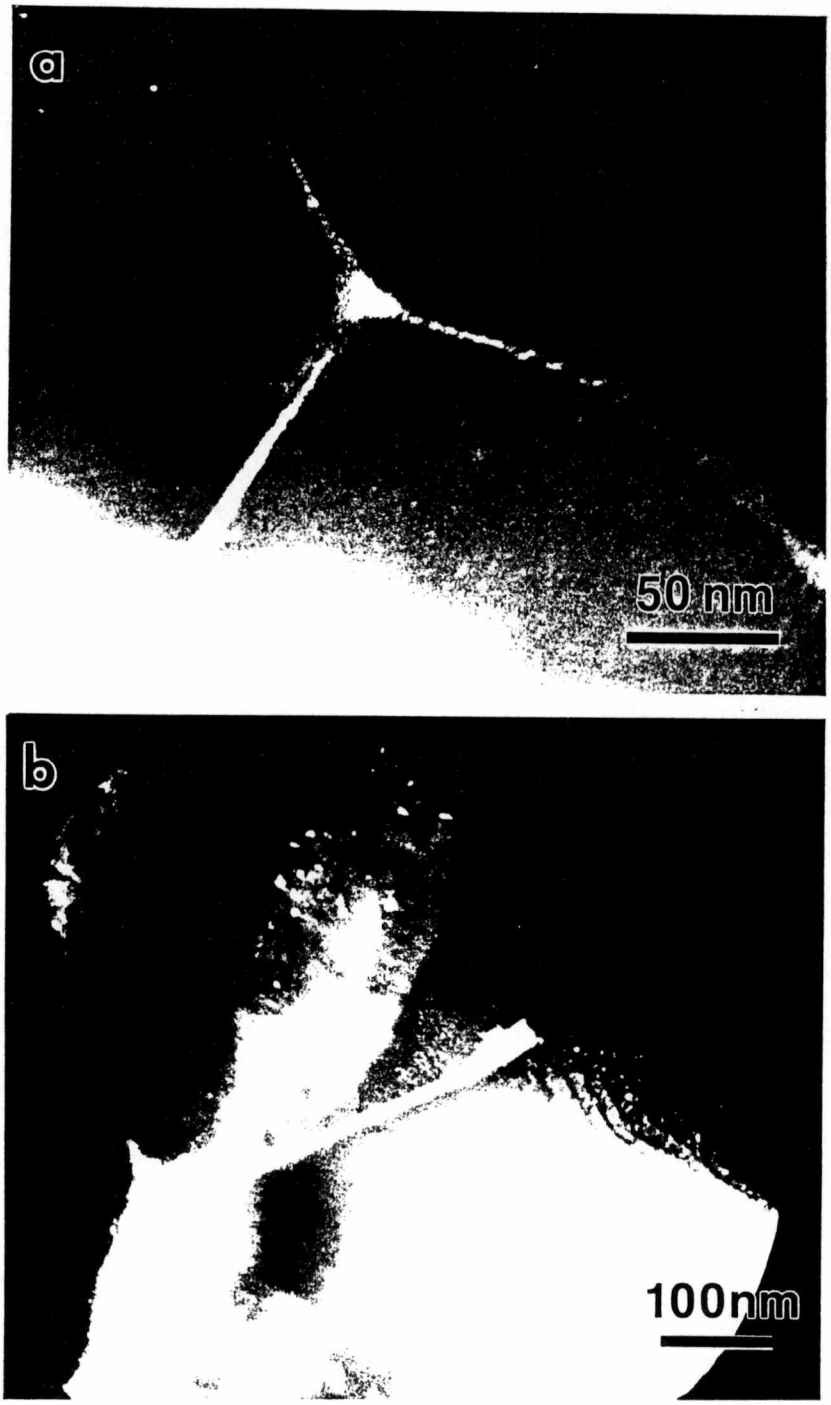

Figure 4.13 TEM dark field images of alumina grain boundaries surrounded by amorphous layers. Samples were sintered at (a) 1650°C and (b) 1550°C, respectively, for 20 min. Note that the melting point of alumina is 2045°C.

400 to 500°C above the sintering temperatures used in this investigation. This experimental observation is a direct evidence to the microwave sintering model suggested by Zhang et al [16] which proposed that at the interfacial necking area the local melting temperature is decreased. This phenomenon is believed to be directly responsible for the reported low value of activation energy of microwave sintering [19].

TEM examinations also revealed that some dislocation arrays appeared in some small angle grain boundaries (Figure 4.14).

4.3.1 Grain Size

Grain growth was suppressed in the microwave sintered samples (see Figure 4.15). Ultrafine grain size dominated although occasionally abnormal grains were observed (Figure 4.16). It is believed that the ultrafine grain size is directly related to the internal heating mechanism of microwave sintering to produce the condition of fast sintering (discussed in section 4.2.1). The origin of the abnormal grains is not fully understand. There are several possibilities that could lead to the condition of their growth. One possibility arises from the existence of a wide initial particle size distribution (see Figure 4.1). From Hillert's criterion, the condition for obtaining stable normal grain growth is that the size of the largest grain must be less than twice the mean size [93]. Another possible cause is the inhomogeneous densification of the green sample. Some common origins of micro-inhomogeneity are: original particle hard agglomeration which could not be broken down during blending; poor packing; and the existence of pressure gradients during die

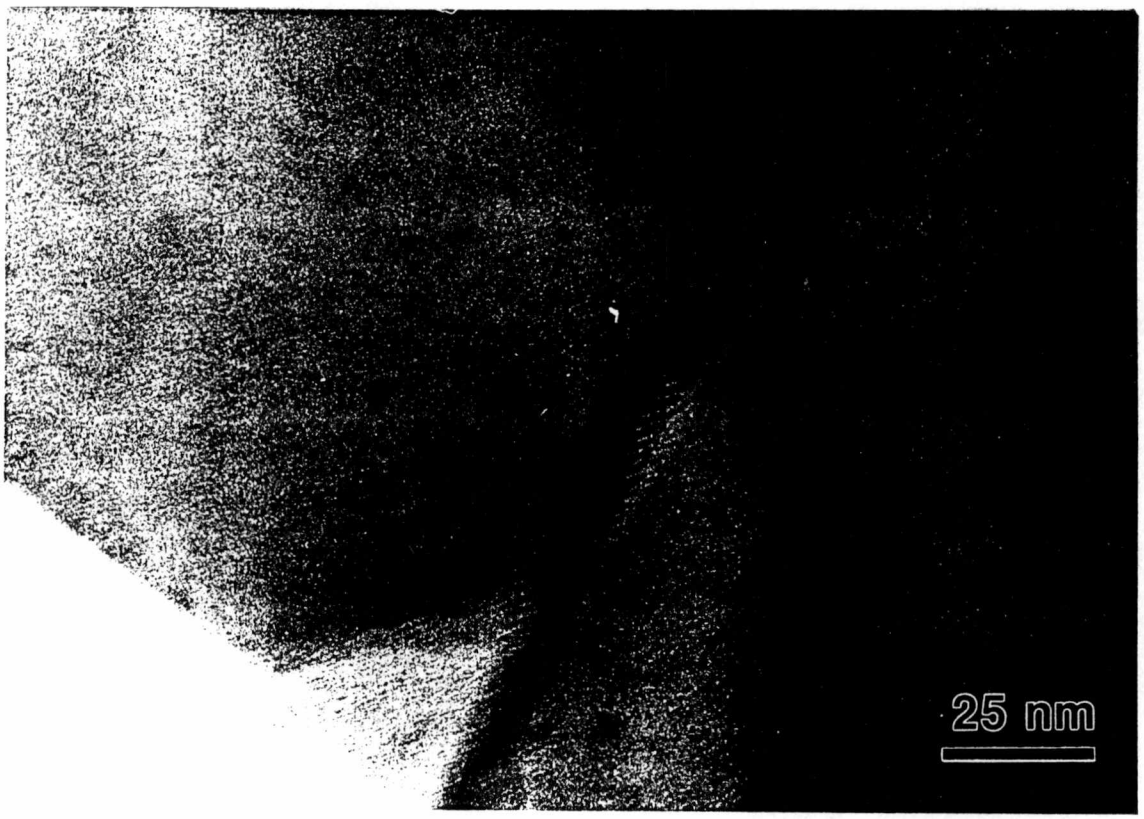

Figure 4.14 A dislocation array located at a small angle grain boundary of alumina matrix.

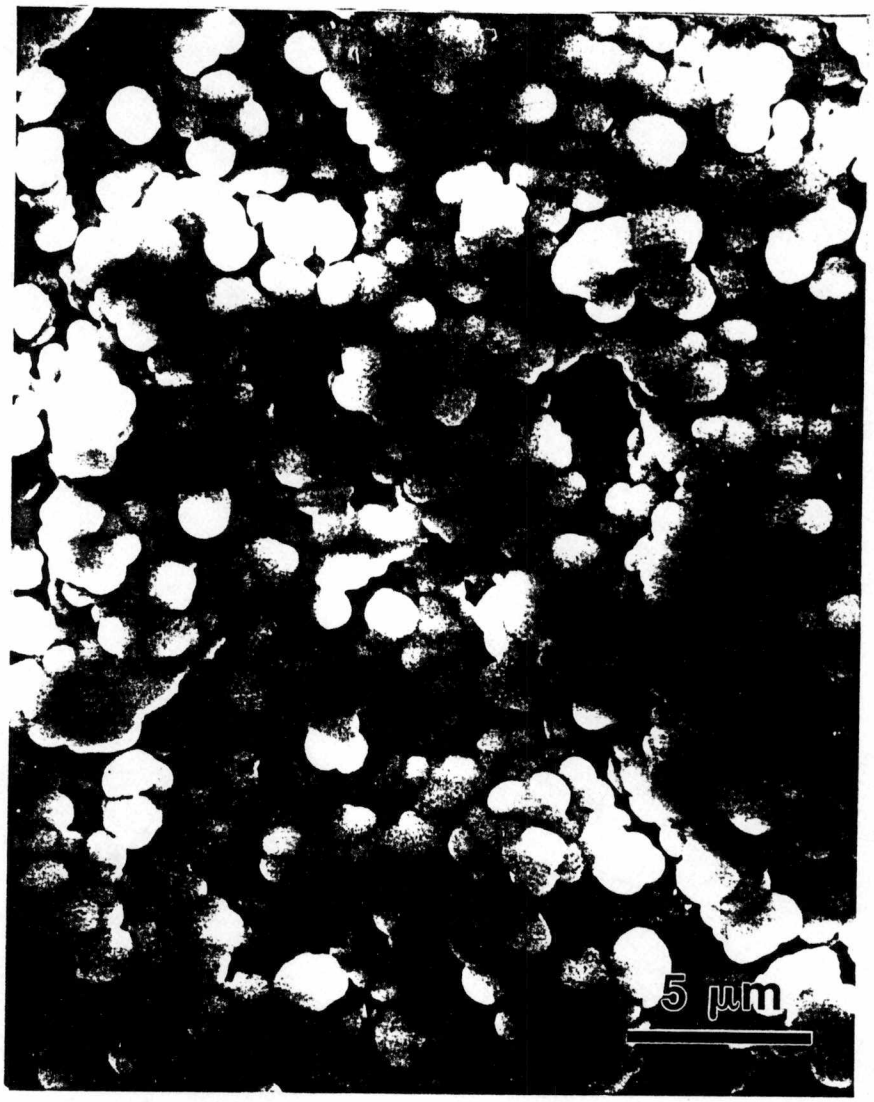

Figure 4.15 SEM fractograph of the specimen sintered at 1550°C for 30 min. Note that there is no or very small grain growth under microwave sintering condition.

Figure 4.16 Abnormal grain growth was occasionally observed.

pressing [95, 96]. As proposed by Meek [13], the region that has more air becomes a preferential interaction spot with the microwaves and creates a precondition for exaggerated grain growth. Some small pores were found within the abnormal grain size (Figure 4.17). The existence of the small pores might be evidence that the large grain was formed from hard agglomeration of green particles.

4.3.2 Interfacial Structure

Figure 4.18 shows the existence of an amorphous interphase at the whisker/matrix interface produced during processing. The contrast at the contacting interface confirms the presence of residual thermal stresses. A convergent electron probe (probe size was about 80 Å) was stepped across the interface and an EDS series spectrum was recorded at each position. Oxygen, silicon, and aluminum signals were collected at each step during the scan. Figure 4.19 shows the concentration distribution of different elements as a function of distance from the whisker to the matrix at two different sintering temperatures.

The amorphous interphase was apparently an aluminosilicate glass. The oxygen concentration rises sharply at the interphase on the SiC_w side and reaches a high level in the middle of the interphase region, and finally drops to a stoichometric level (Al_2O_3) at the interphase on the side of Al_2O_3 matrix. The specimen sintered at 1550°C had a much higher oxygen concentration (about 14 wt% higher) in the interphase region than that sintered at 1650°C, which implied that a stronger interface reaction was involved. The silicon

Figure 4.17 Small pores were found in some of the abnormally grown alumina grains.

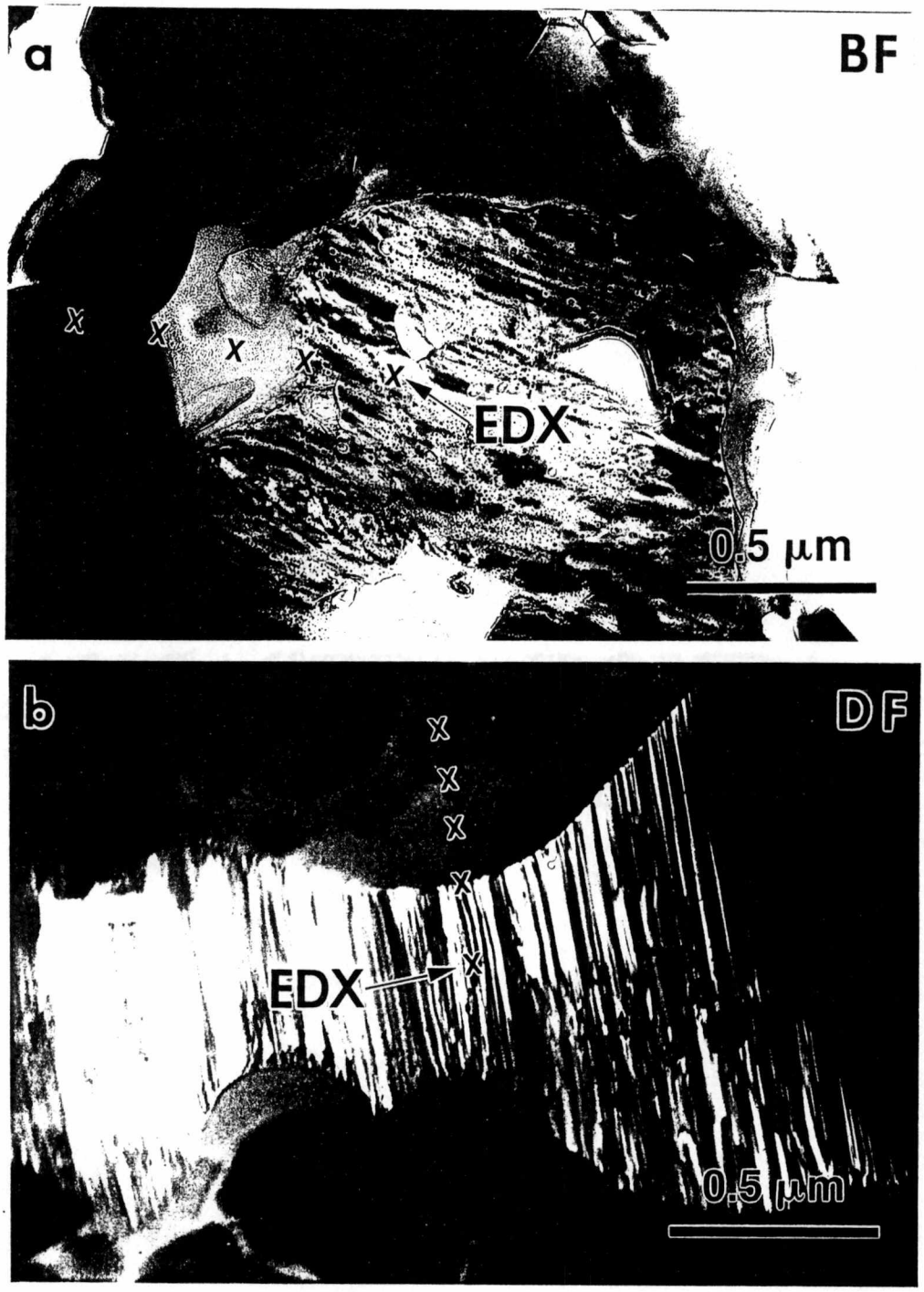

Figure 4.18 Amorphous interphases exist in whisker-matrix interface of CMCs. Samples were sintered at (a) 1650°C and (b) 1550°C, respectively, for 20 min.

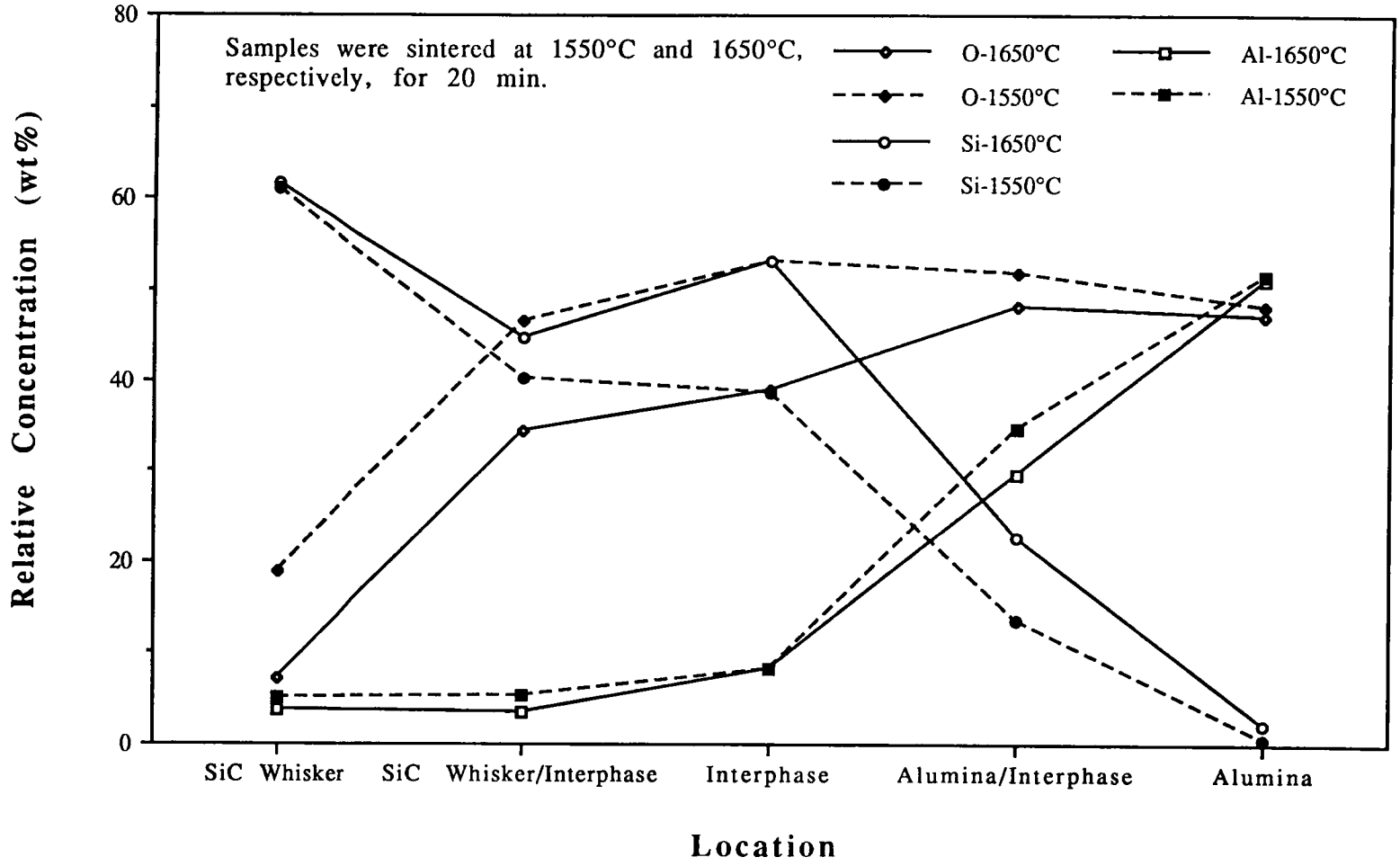

Figure 4.19 Results of EDX microanalysis across the interphase region for the samples sintered at two different temperatures.

concentration exhibited a decreasing profile from the SiC_w to the Al_2O_3 matrix. The specimens sintered at 1650°C showed a higher Si level (about 14 wt% higher) in the middle of the interphase region. The aluminum concentration gradually built up in the interphase region close to the side of Al_2O_3 matrix. The specimen sintered at 1550°C had a slightly higher aluminum level (about 5 wt%) on the side of the alumina matrix, which again implied that more alumina joined the interaction at that temperature. Over all, it seems that a stronger interface interaction occurred at 1550°C, which might be favored by the thermodynamic condition.

The origin of the amorphous layer is believed to be the product(s) of the interaction(s) between the SiO_2 layer (about 20 nm thick) on the SiC_w surface and the Al_2O_3 matrix. The existence of the SiO_2 layer on the surface of the SiC_w was verified from XPS analysis and TEM analysis, and it has also been reported by various authors [46, 88, 97]. The amorphous interphase of samples sintered at 1550°C could create a relatively "stronger" interface and may be more difficult to debond under stress than a relatively "weaker" interface possessed by samples sintered at 1650°C [98]. This microanalytical result provides a reasonable explanation for the difference in the fracture toughness data for these two different sintering conditions (Table 4.4).

4.3.3 Phase Analysis

An example of an X-ray diffraction pattern from the composite is shown in Figure 4.20. Only the α-Al_2O_3 phase was detected along with evidence that a small fraction of the α-Al_2O_3 had been

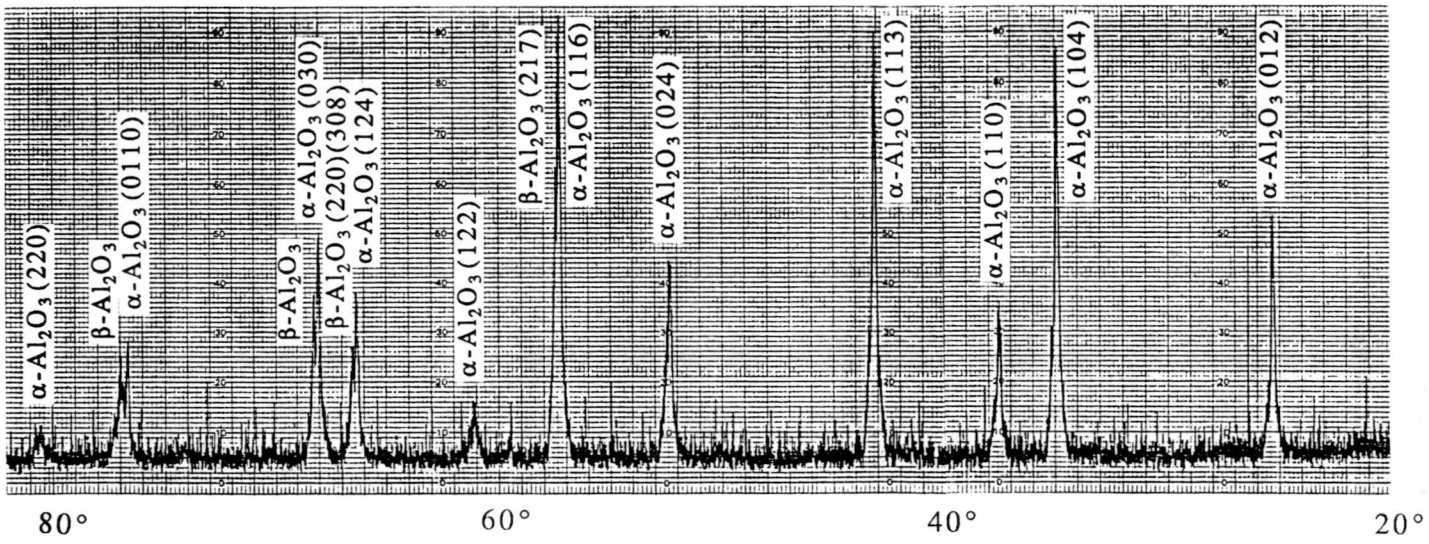

Figure 4.20 An example of XRD pattern of the microwave sintered CMC. Note the existence of a small amount of β-Al_2O_3 phase.

transformed to β-Al_2O_3. No SiC (about 0.2 wt% in the composite) or any other possible reaction products were detected by this technique.

4.4 CMC Toughening Mechanisms

4.4.1 Toughening Phenomena Observed from Indentation Tests

Through observation of the crack trace created by the indenter, it was not difficult to find that all whisker toughening mechanisms, such as crack deflection around whiskers (Figure 4.21), whisker debonding (Figure 4.22), and whisker bridging across the crack (Figure 4.23), were operative in the microwave sintered SiC_w-Al_2O_3 CMCs. Crack deflection was the most common phenomenon observed in all samples.

In Figure 4.21(a) the crack was deflected by about 40° along a whisker lying on the polished surface; while Figure 4.21(b) showed a crack deflection along the edge of the whisker oriented perpendicular to the polished surface. Note that there is apparently an interphase layer surrounding the whisker, which is consistent with the TEM observation.

It was also evident that in some degree the matrix self-toughening mechanism (for example, grain bridging across the crack, see Figure 4.24) was also operative [99].

4.4.2 Toughening Phenomena Observed from Fracture Surfaces

On the fracture surface, the long angular cavity that appeared to be left behind following whisker pullout (indicated by arrows in Figure 4.25) and protrusions of whiskers (Figure 4.26) were evidence

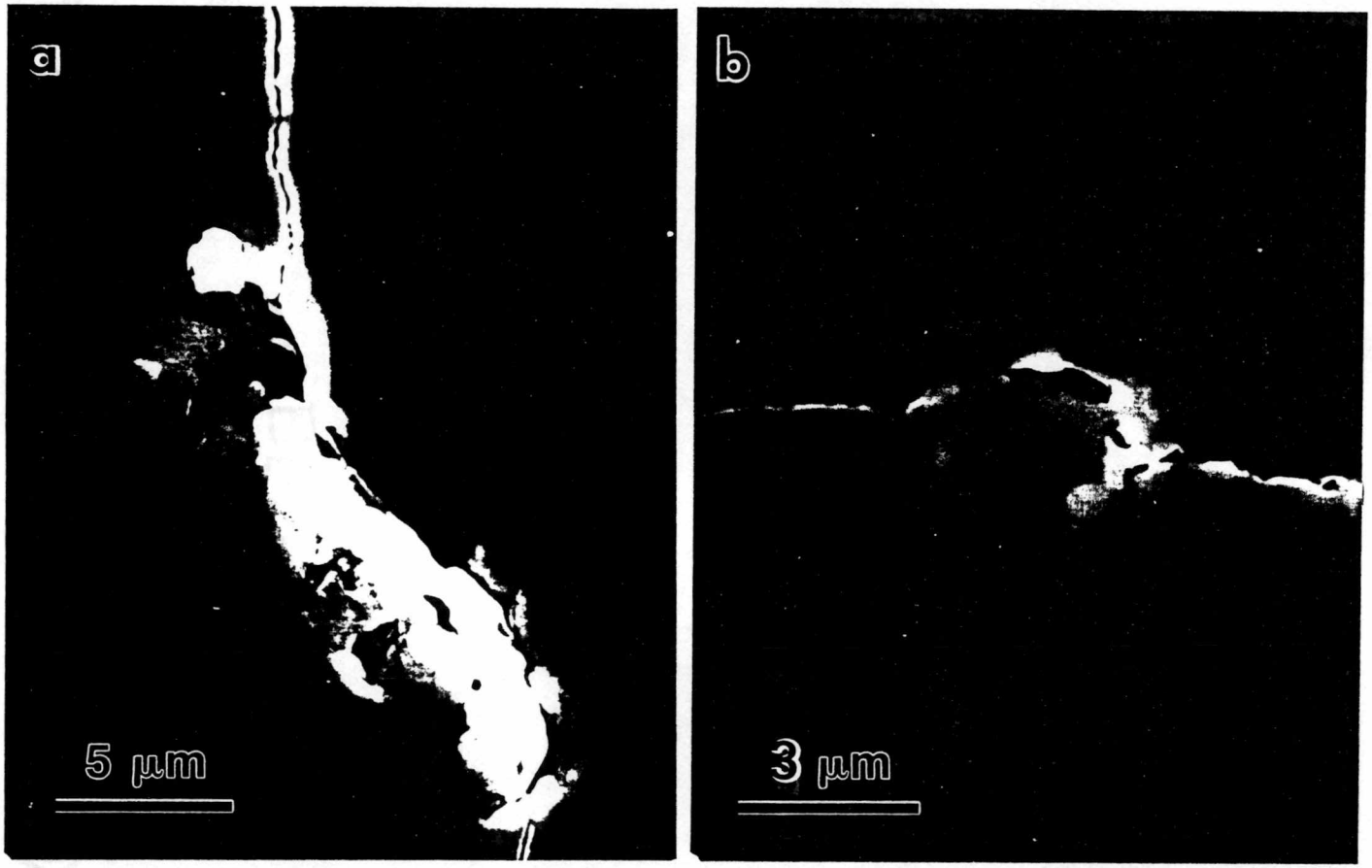

Figure 4.21 SEM micrographs show cracks deflected around the SiC whiskers. (a) A crack was deflected by about 40° along a whisker lying on the polished surface; (b) a crack was deflected along the edge of the whisker oriented perpendicular to the polished surface.

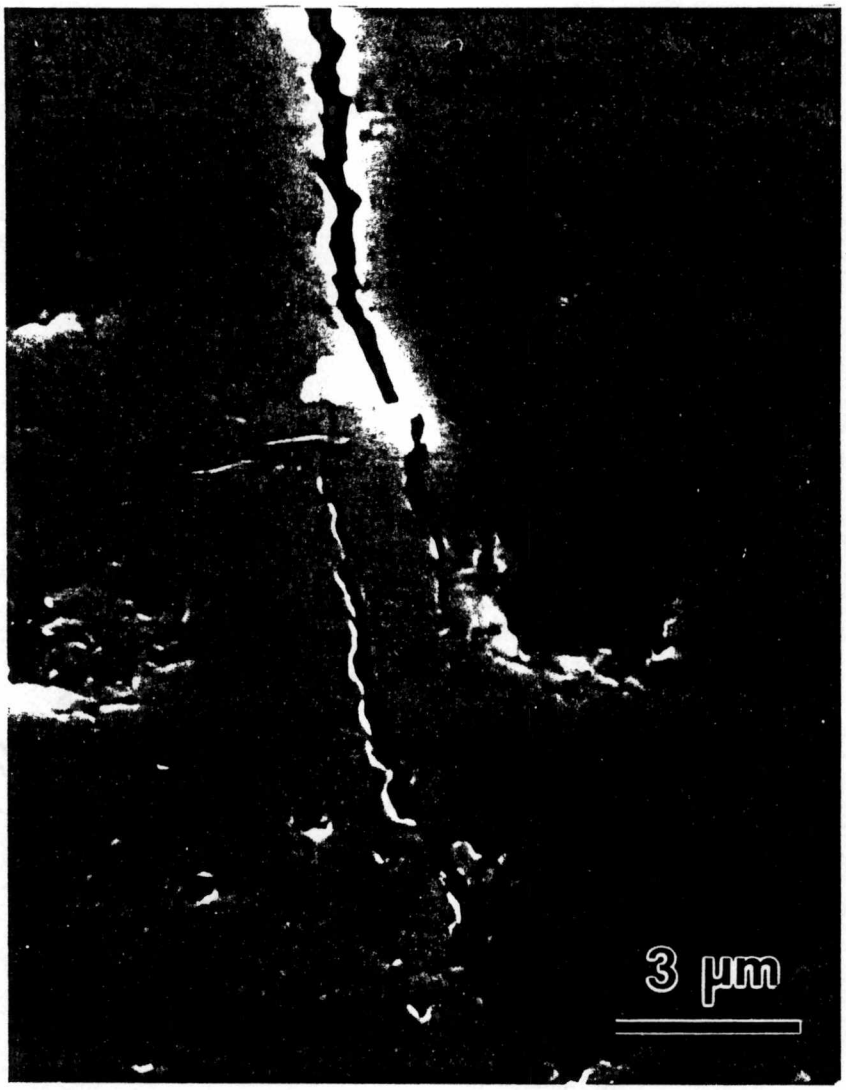

Figure 4.22 SEM micrograph shows a whisker debonded from the matrix as the result of the crack propagation.

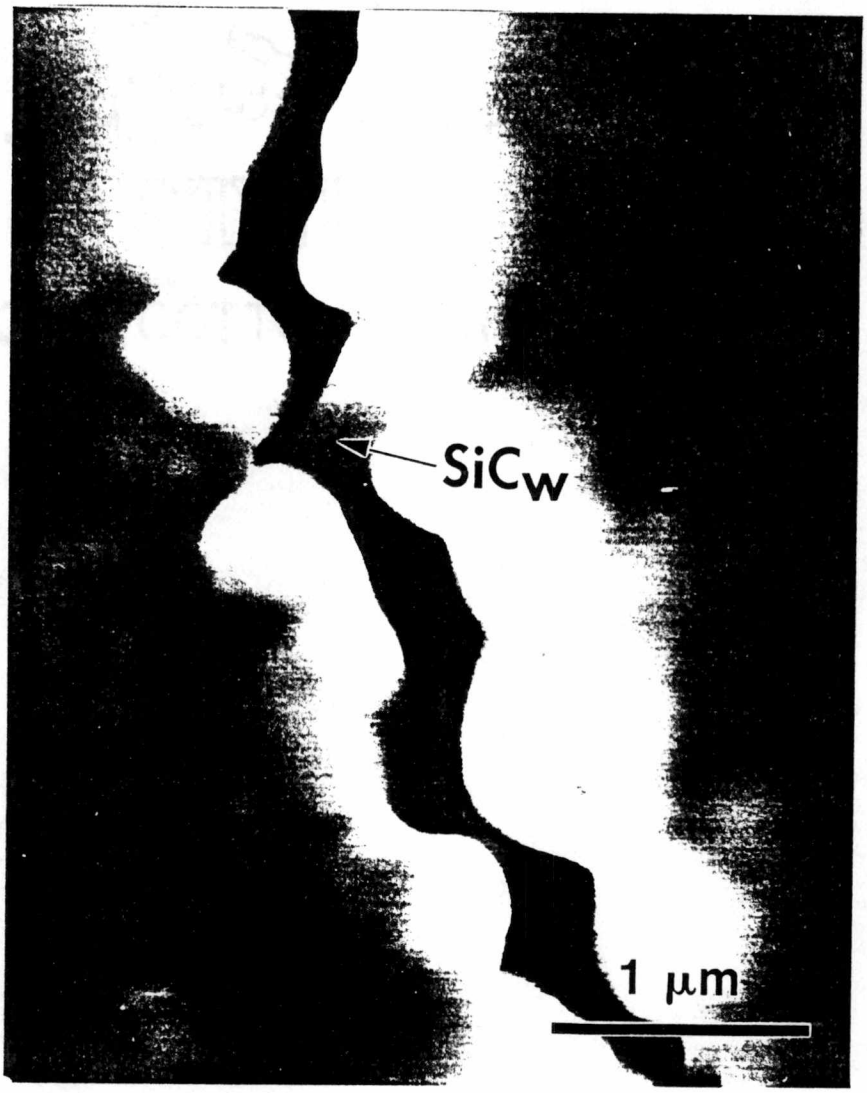

Figure 4.23 SEM micrograph shows a whisker was bridged across the crack.

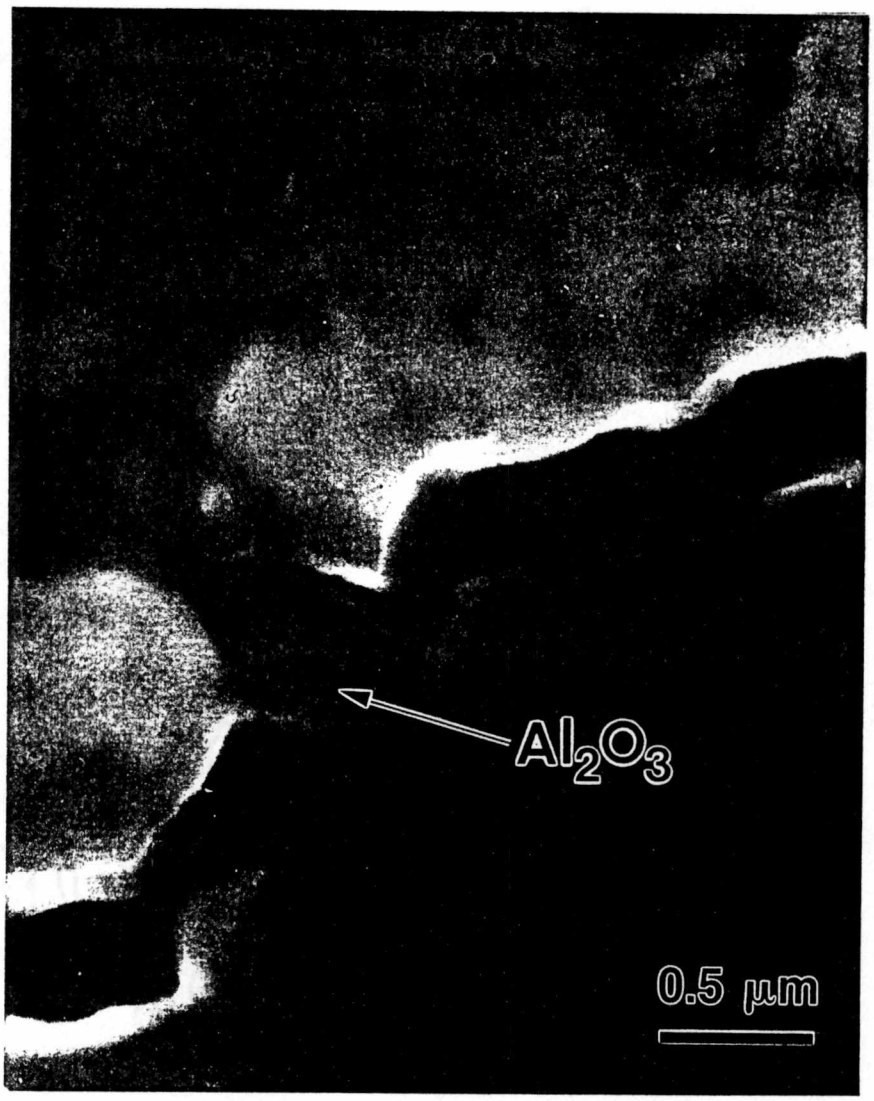

Figure 4.24 SEM micrograph shows the existence of grain bridging across the crack, a matrix self-toughening mechanism.

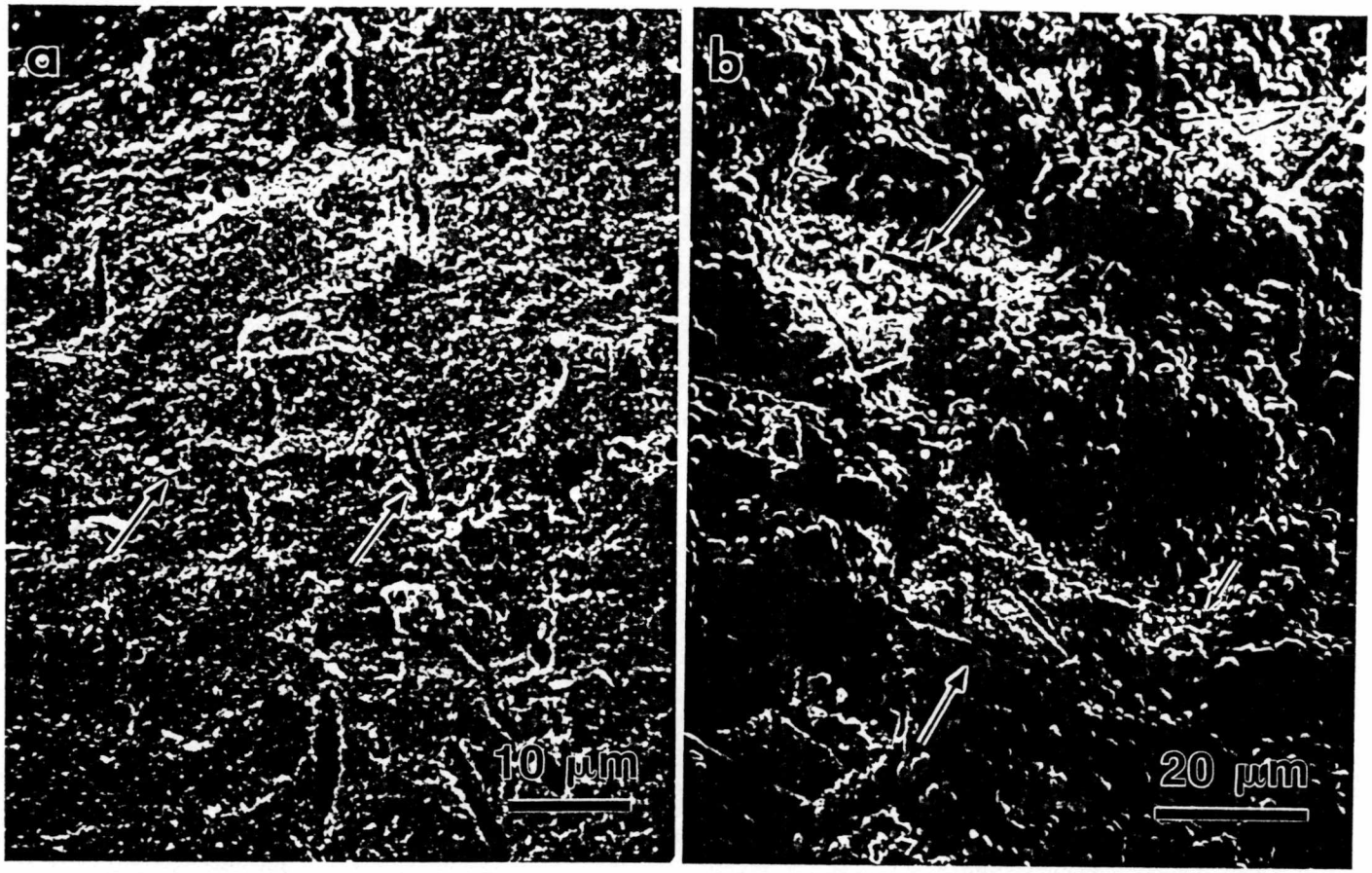

Figure 4.25 SEM fractographs of the fracture surfaces of the CMCs. Samples were sintered at (a) 1650°C and (b)1550°C, respectively, for 30 min.

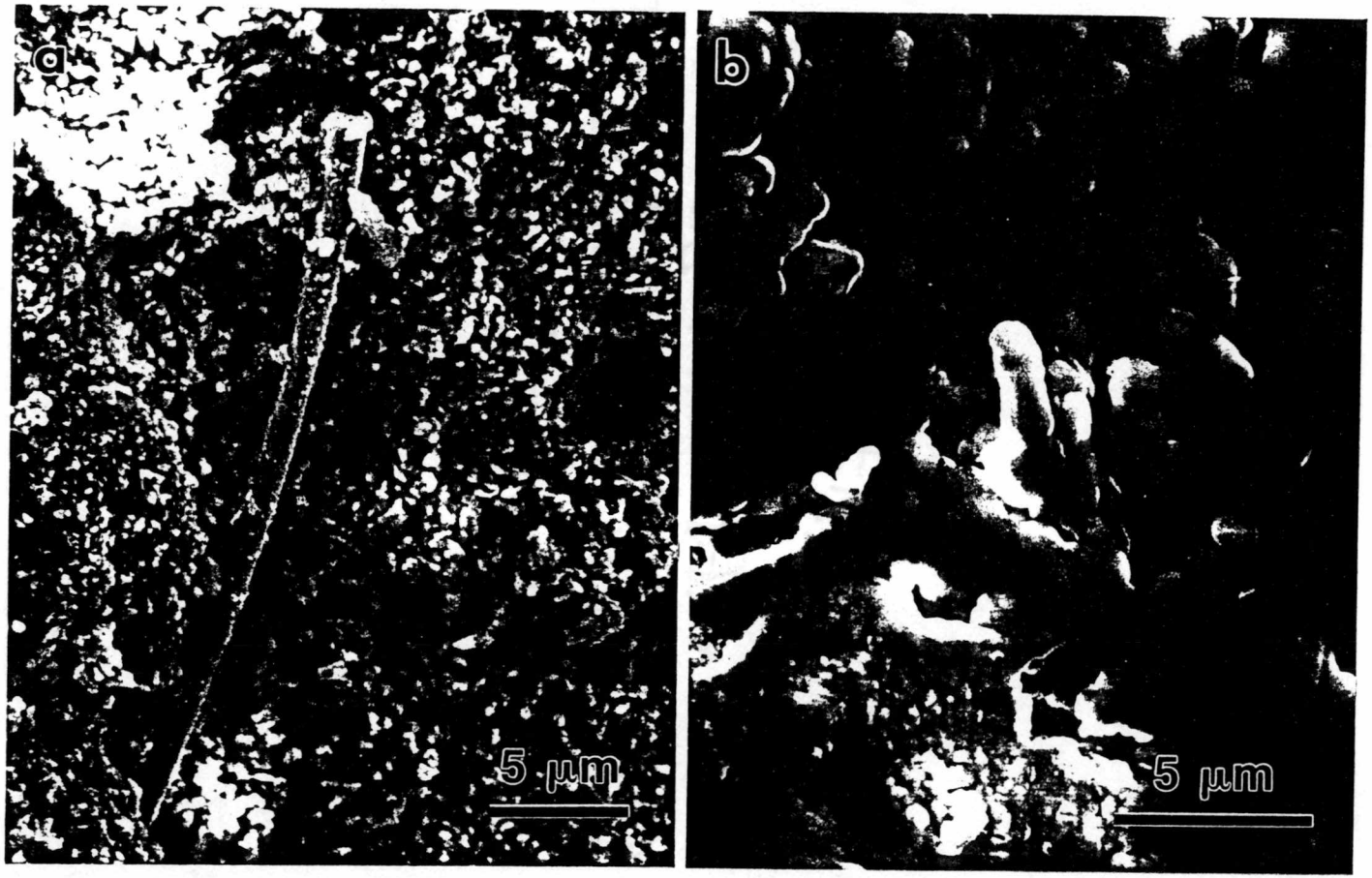

Figure 4.26 SEM fractographs show the whisker-pull-out phenomenon. Samples were sintered at (a) 1650°C and (b)1550°C, respectively, for 30 min.

of whisker pullout. Deflection of cracks by the whiskers also appeared to be operative (Figure 4.27).

In Figure 4.25(a) it is obvious that whiskers were pulled out in orientations of both parallel and perpendicular to the fracture surface of the sample sintered at 1650°C for 30 min. Figure 4.25(b) represents the fracture surface of the specimen sintered at 1550°C for the same amount of time. By comparing (a) and (b), it is clear that the sample sintered at 1650°C showed a greater degree of whisker pullout. The whisker pullout length is also different for samples sintered at the different temperatures. Figure 4.26(a) shows a pullout length of about 30 μm for the sample sintered at 1650°C compared with a length of 3 μm for the sample sintered at 1550°C (Figure 4.26(b)).

The above observations were consistent with the measured fracture toughness data for these samples. In general, the samples sintered at 1550°C had about 10% lower values of fracture toughness than those samples sintered at 1650°C.

From the fractographs (Figure 4.27) it appeared that the fine-grained composites displayed intergranular crack propagation. Figure 4.28 suggested that the whisker cluster was the origin of the crack.

4.4.3 Toughening Mechanisms

From the above observations, it is believed that the increase in fracture toughness of microwave sintered SiC whisker-reinforced alumina composites was mainly due to the crack deflection mechanism. This mechanism assumes that the crack initiates in the matrix and expands around the whiskers. As the crack changes its

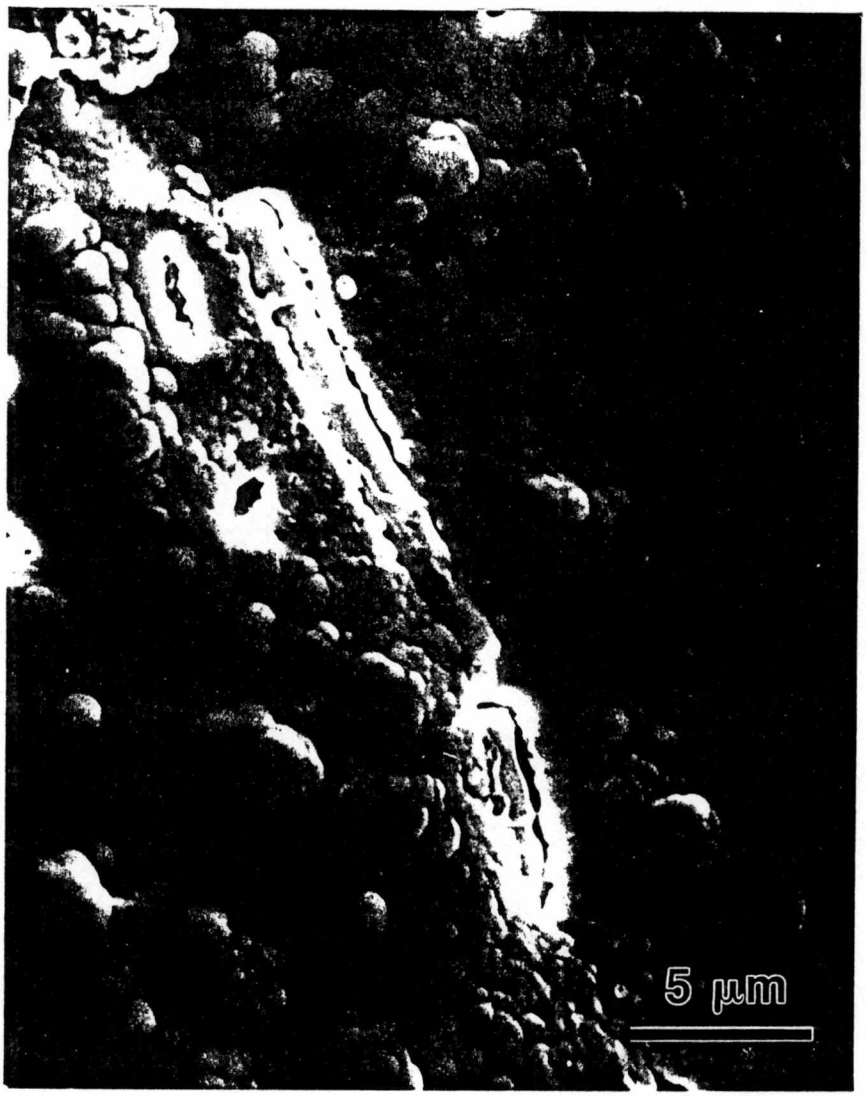

Figure 4.27 SEM fractograph shows crack deflection along the SiC whisker edges.

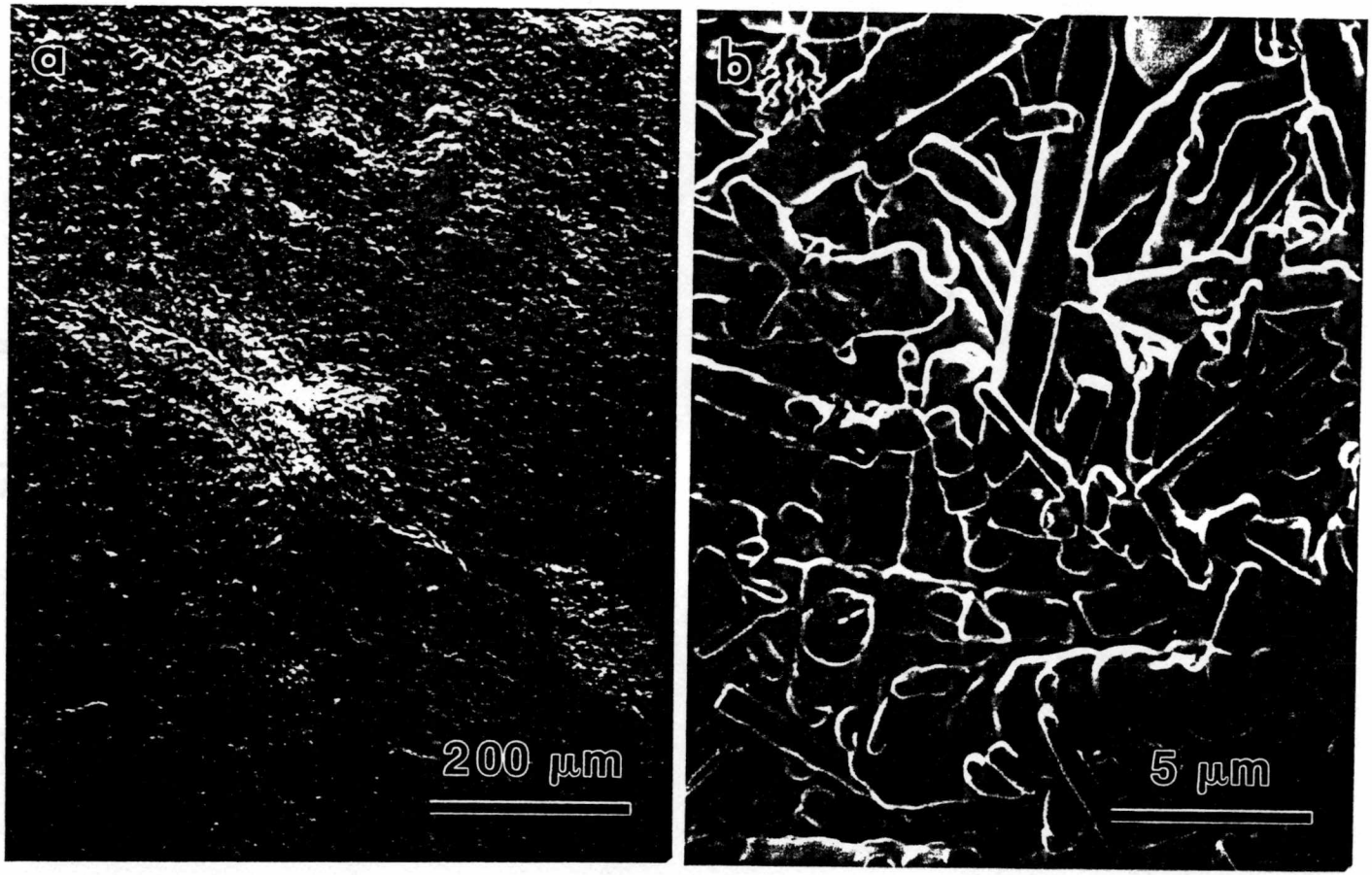

Figure 4.28 (a) SEM fractograph of a whisker cluster which was apparently the origin of the crack; (b) an enlarged view of the whisker cluster.

direction, its orientation relative to the applied stress will change and it will therefore require more energy to extend further, and hence the fracture toughness of the material is increased.

Whisker debonding, whisker bridging, and whisker pullout mechanisms were all operative in large degrees among the sintered samples. Due to the fine grain size of the matrix, grain-bridging toughening was also observed. It is believed that the existence of an amorphous interphase between the whisker and the matrix facilitates the weak bonding between them and at least at room temperature it leads to improvement of fracture toughness of the composites.

4.5 Characteristics of Microwave Sintering of CMCs

The observed fast sintering rate is the major attraction for continued development of microwave processing for ceramic composites. The short sintering time with remarkable improvement of the mechanical properties of the materials makes microwave sintering suitable for processing of ceramic composites.

Ultrafine grain size is a distinguishing characteristic of the microwave sintered composite. This could be the result of (1) the rapid heating in the microwave field, and (2) SiC whisker-inhibited grain growth during the sintering. In this case, the second reason was not likely due to the small amount of SiC whiskers (10 vol%) in the matrix. The fine grain size facilitates the densification process of the composite. The fine grain size also would affect the mechanical properties of the materials.

The presence of a liquid phase during microwave sintering of

the composite provides an extra benefit to the improvement of the fracture toughness. The amorphous interface is apparently at least in part responsible for the low values of elastic modulus of the composite which inevitably contributes to the increase in the fracture toughness. The liquid phase also speeds the densification process.

4.6 Conclusions

(1) Microwave sintered silicon carbide whisker (10 vol%) reinforced alumina matrix composite showed a significant improvement of fracture toughness over conventionally sintered monolithic alumina. The fracture toughness was measured by an indentation method.

(2) Crack deflection along the whiskers was the major toughening mechanism operating in the composite. However, whisker bridging, whisker debonding, and whisker pullout all contributed to the increase in fracture toughness of the composite. The grain-bridging toughening was also observed.

(3) The interfacial bonding between the whiskers and the alumina matrix played an important role in the composite materials. The bonding is related to either a mechanical bond caused by the thermal expansion mismatch or a chemical bond caused by the chemical interaction between the whisker and the alumina matrix.

(4) An amorphous interphase between whisker and matrix contributed to a weak interface. The nature of the interphase is thought to be an aluminosilicate glass phase.

(5) Strong interface interactions between the whiskers and the alumina matrix weakened the benefits of the whisker toughening effects. Samples sintered at 1650°C showed a 10% higher toughness than those sintered at 1550°C where a strong interface interaction was obvious.

(6) Without sintering aids, the microwave sintered composites reached a high density ranging from 97 to 99.5% within 30 min.

(7) Ultrafine grain size was a characteristic of the microwave sintered composites, which was directly related to the microwave internal volumetric sintering mechanism.

(8) The presence of thin amorphous layers distributed uniformly along most of the Al_2O_3 grain boundaries were vivid evidence of reduction of the grain boundary melting temperature due to the presence of the electromagnetic field. The presence of the liquid phase during sintering facilitated the densification process and was directly responsible for the apparent decrease of activation energy [19]. The existence of the amorphous layer between the grains was believed to be responsible at least in part for the low values of the elastic moduli measured by the pulse-echo method.

BIBLIOGRAPHY

BIBLIOGRAPHY

1. M. A. Janny and H. D. Kimrey, pp. 919 in Ceram. Trans., Ceramic Powder Science II, Vol 1, 1987

2. T. T. Meek, R. D. Blake, and J. J. Petrovic, Ceram. Eng. Sci. Proc., **8** [7-8] 861 (1987).

3. Berta Stwain, Microwave Sintering of Ceramics, Advanced Materials and Processes Inc., Metal Progress, 1988

4. L. M. Sheppard, Am. Ceram. Soc. Bull., **67** [10] 1656 (1988).

5. W. R. Tinga, Design Principles for Microwave Heating and Sintering, pp. 105, Mater. Res. Soc., Pittsburgh, PA, 1988

6. W. R. Tinga and S. O. Nelson, J. Microwave Power, **8** [1] 23 (1973)

7. A. C. Metaxas and R. J. Meredith, Industrial Microwave Heating, Peter Peregrinus Ltd., 1983

8. A. Von Hippel edited, Dielectric Materials and Applications, The Technology Press of MIT and John Wiley and Sons, Inc., New York, 1961

9. J. D. Walton, Jr., pp. 229 in Randome Engineering Handbook, Edited by J. D. Walton, Jr., Marcel Dekker, Inc., New York, 1970

10. W.W. Ho, pp. 137 in Microwave Processing of Materials, Edited by W. H. Sutton, M. H. Brooks, and I. J. Chabinsky, Mater. Res. Soc., Pittsburgh, PA, 1988

11. W. H. Sutton, Am. Ceram. Soc. Bull., **68** [2] 376 (1989).

12. J. M. Osepchuk, IEEE Trans., Microwave Theory Tech., **MIT-32** [9] 1200 (1984)

13. T. T. Meek, J. Mater. Sci. Lett., **6**, 638 (1987)

14. D. L. Johnson and R. R. Rizzo, Am. Ceram. Soc. Bull., **59** [4] 467 (1980)

15. M. A. Janney, H. D. Kimrey, M. A. Schmidt, and J. O. Kiggans, J. Am. Ceram. Soc., **74** [7] 1675 (1991)

16. T. T. Meek, X. Zhang, and M. Rader, pp. 81 in Microwaves : Toeory and Application in Materials Processing, Edited by D. A. Clark, F. D. Gac, and W. H. Sutton, Am. Ceram. Soc., Inc., Westerville, OH, 1991

17. W. H. Tinga, pp. 33 in Microwave Processing of Materials, Edited by W. H. Sutton, M. H. Brooks, and I. J. Chabinsky, Mater. Res. Soc., Pittsburgh, PA, 1988

18. M. Kus and V. M. Kenkre, Phys. Rew., **45** [17] 9695 (1992)

19. M. A. Janney and H. D. Kimrey, Advances in Sintering, Edited by J. Bleninger and C. Handwerker, Am. Ceram. Soc., Inc., Westerville, OH, 1990

20. M. F. Iskander, pp.149 in Microwave Processing of Materials II, Edited by W. B. Snyder, Jr., W. H. Sutton, M. F. Iskander, and D. L. Johnson, Mater. Res. Soc., Pittsburgh, PA, 1991

21. V. M. Kenkre, L. Skala, M. W. Weiser, and J. D. Katz, *ibid*, pp. 179

22. E. E. Eves II and R. L. Snider, *ibid*, pp. 201

23. M. F. Iskander, O. Andrade, H. Kimrey, R. Smith, and S. Lamoreaux, pp. 141 in Microwaves : Theory and Application in Materials Processing, Edited by D. A. Clark, F. D. Gac, and W. H. Sutton, Am. Ceram. Soc., Inc., Westerville, OH, 1991

24. C. Lorenson and C. Gallerneault, *ibid*, pp. 193

25. J. D. Ford and D. C. T. Pei, J. Microwave Power, **2** [2] 61 (1967)

26. R. Roy, S. Komarneni, and L. J. Yang, J. Am. Ceram. Soc., **68** [7] 392 (1985)

27. P. A. Haas, Am. Ceram. Soc. Bull., **58** [9] 873 (1979)

28. K. D. Humphrey, Microwave Sintering of $BaTiO_3$, M.S. Thesis, University of Missouri-Rolla, 1980

29. M. K. Krage, Am. Ceram. Soc. Bull., **60** [11] 1232 (1981)

30. D. Katz, R. D. Blake, J. J. Petrovic, and H. Sheinberg, pp. 219 in Microwave Processing of Materials, Edited by W. H. Sutton, M. H. Brooks, and I. J. Chabinsky, Mater. Res. Soc., Pittsburgh, PA, 1988

31. D. Katz, R. D. Blake, J. J. Petrovic, and C. P. Scherer, Ceram. Eng. Sci. Proc., **10** [7-8] 857 (1989)

32. J. Wilson and S. Kunz, Microwave sintering of Partially stabilized Zirconia, Presented at the 89th Annual Meeting of the American Ceramic Society, Pittsburgh, Pa, April 30. 1987 (Engineering Ceramic Division, Paper No. 172-C-87)

33. J. F. MacDowell, Microwave Heating of Nepheline Glass-Ceramics, Am. Ceram. Soc. Bull., **63**, 282 (1984)

34. M. A. Janny and H. D. Kimmrey, pp. 919 in Powder Science II, B. Edited by G. L. Messing, E. R. Fuller, Jr., and H. Hausner, Am. Ceram. Soc., Westerville, OH, 1988

35. F. Okada, S. Tashiro, and M. Suzuku, pp. 201 in Advances in Ceramics, Vol.15, International Conference on Ferrites, Part I, Edited by F. Y. Wang, Am. Ceram. Soc., Westerville, OH, 1988

36. V. K. Varadan, Y. Ma, A. Lakhtakia, and V. V. Varadan, pp. 45 in Microwave Processing of Materials, Edited by W. H. Sutton, M. H. Brooks, and I. J. Chabinsky, Mater. Res. Soc., Pittsburgh, PA, 1988

37. T. N. Tiegs, J. O. Kiggans, and H. O. Kimrey, Ceram. Eng. Sci. Proc. **12** [9-10] 1981 (1991)

38. R. W. Rice, Ceram. Eng. Sci. Proc., **11** [7-8] 667 (1990)

39. S. T. Buljan, A. E. Pasto, and H. J. Kim, Am. Ceram. Soc. Bull., **68** [2] 387 (1989)

40. R. A. J. Sambell et al., J. Mater. Sci. **7** 676 (1972)

41. P. F. Becher and G. C. Wei, J. Am. Ceram. Soc., [12] C-267 (1984)

42. J. Liu and P. D. Ownby, J. Am. Ceram. Soc., **74** [3] 674 (1991)

43. R. C. Garvie, R. H. Hannink, and R. T. Pascoe, Nature, **258**, 703 (1975)

44. A. G. Evans, Mater. Sci. and Eng., **A105/106**, 65 (1988)

45. M. D. Thouless and A. G. Evans, Acta Metall., **36** [3] 517 (1988)

46. P. F. Becher et al., J. Am. Ceram. Soc., **71** [12] 1050 (1988)

47. P. F. Becher, Annu. Rev. Mater. Sci., **20**, 179 (1990)

48. P. F. Becher, J. Am. Ceram. Soc., **74** [2] 255 (1991)

49. K. Jakus and S. V. Nair, Composites Science and Technology, **37**, 279 (1990)

50. M. T. Sykes et al., Composites, **18** [2] 153 (1987)

51. P. F. Becher, pp. 137 in Advanced Ceramics II, Edited by S. Somiya, Elsevier Applied Science, London and New York, 1986

52. A. E. Giannakopoulos and K. Breder, J. Am. Ceram. Soc., **74** [1] 194 (1991)

53. A. G. Evans and K. T. Faber, J. Am. Ceram. Soc., **67** [4] 255 (1984)

54. J. H. Hutchinson, Acta Metall., **35** [7] 1605 (1987)

55. A. G. Evans, J. Am. Ceram. Soc., **73** [2] 187 (1990)

56. G. H. Campbell et al., J. Am. Ceram. Soc., **73** [3] 521 (1990)

57. K. T. Faber and A. G. Evans, Acta Metall., **31** [4] 565 (1983)

58. M. Rühle, B. J. Dalgleish, and A. G. Evans, Scr. Metall., **21** [5] 681, (1987)

59. D. B. Marshall and A. G. Evans, Mater. Forum, **11**, 304 (1988)

60. H. Kleebe et al., Proc. Mater. Res. Soc. Symp., **170**, 79 (1990)

61. T. N. Tiegs and P. F. Becher, Am. Ceram. Soc. Bull., **60** [2] 339 (1987)

62. D. E. Wittmer, Ceram. Eng. Sci. Proc., **9** [7-8] 735 (1988)

63. J. Nomeny and C. Mangin, pp. 229 in Interfaces in Composites, Edited by C. G. Pantano and E. J. H. Chen, Mater. Res. Soc., Pittsburgh, PA, 1988

64. A. A. Morrone, S. R. Nutt, and S. Suresh, J. Mater. Sci., **23**, 3206 (1988)

65. K. Xia and T. G. Langdon, pp. 85 in Metallography of Advanced Materials, Edited by H. J. Cialone et al., IMS and AMS, 1988

66. T. N. Tiegs and P. F. Becher, pp. 639 in Tailoring Multiphase and Composite Ceramics, Edited by R. E. Tressler et al., Plenum Press, New York and London, 1986

67. G. C. Wei and P. F. Becher, Am. Ceram. Soc. Bull., **64** [2] 298 (1985)

68. T. Ishii and H. K. Bowen, pp. 452 in Ceramic Tansactions, Vol. 1, Edited by G. L. Messing, E. R. Fuller, and H. Hausner, Am. Ceram. Soc., Inc., Weaterville, OH, 1988

69. M. D. Sacks, H. W. Lee, and O. E. Rojas, Ceram. Eng. Sci. Proc., **9** [7-8] 741 (1988)

70. K. J. Konsztowicz, Ceram. Eng. Sci. Proc., **11** [7-8] 695 (1990)

71. Y. W. Kim and J. G. Lee, J. Mater. Sci., **26**, 1316 (1991)

72. M. J. Hoffmann et al., J. Am. Ceram. Soc., **72**, 765 (1989)

73. C. H. Hsueh, *ibid*, **71**, C442 (1988)

74. P. Lipetski, S. R. Nutt, and P. F. Becher, pp. 271 in High Temoerature/High Performance Composites, Edited by F. D. Lemkey et al., Mater. Res. Soc., Pittsburgh, PA, 1988

75. D. S. Liu and A. Parvizi-Majidi, Ceram. Eng. Sci. Proc., **11** [7-8] 745 (1990)

76. K. Jakus and S. M. Wiederhorn, J. Am. Ceram. Soc., **71** [10] 832 (1988)

77. T. J. Chuang, S. M. Wiederhorn, and S. M. Chen, pp. 957 in Proc. of 3rd Int. Conf. on Creep and Fracture of Engineering Materials and Structures, Edited by B. Wilshire and R. W. Evans, The Institute of Metals, London, 1987

78. A. G. Evans et al., pp. 259 in Advanced Structure Ceramics, Edited by P. F. Becher, M. V. Swain, and S. Somiya, Mater. Res. Soc., Pittsburgh, PA, 1986

79. Y. L. Tian and D. L. Johnson, pp. 925 in Ceramic Poeder Science II, Edited by G. L. Messing, E. R. Fuller, and H. Hausner, Am. Ceram. Soc., Inc., Weaterville, OH, 1988

80. ASTM Standard C 693-84

81. A. G. Evans and E. A. Charles, J. Am. Ceram. Soc., **59**, 371 (1976)

82. B. L. Lawn, A. G. Evans, and D. B. Marshall, J. Am. Ceram. Soc., **63**, 574 (1980)

83. G. R. Anstis et al., J. Am. Ceram. Soc., **64** [9] 533 (1981)

84. K. Niihara, R. Morena, and D. P. H. Hasselman, J. Mater. Sci. Lett., **1**, 13 (1982)

85. M. T. Laugier, *ibid.*, **4**, 1539 (1985)

86. M. T. Laugier, *ibid.*, **5**, 1501 (1987)

87. K. M. Liang, G. Orange, and G. Fantozzi, J. Mater. Sci. **25**, 207 (1990)

88. K. R. Karasek, J. Mater. Sci. **25**, 103 (1991)

89. S. M. Smith et al., J. Am. Ceram. Soc., **72** [7] 1552 (1989)

90. H. D. Kimrey and M. A. Janny, pp. 367 in Microwave Processing of Materials, Edited by W. H. Sutton, M. H. Brooks, and I. J. Chabinsky, Mater. Res. Soc., Pittsburgh, PA, 1988

91. P. R. Buseck, H. M. Cowley, and L. Eyring, High-Resolution Transmission Electron Microscopy and Associated Techniques, Oxford University Press, New York and Oxford, 1988

92. M. Yang and R. Stevens, J. Mater. Sci., **26**, 726 (1991)

93. J. K. Mackenzie, Proc. Phys. Soc., **B63**, 2 (1950)

94. M. Hillert, Acta Met., **13**, 227 (1965)

95. K. Uematsu et al., pp. 190 in Proc. Of Int. Symp. of Factors in Densification and sintering of Oxide and Non-oxide Ceramics, Edited by S. Somiya and S. Salko, 1978

96. J. Hlavac, pp. 264 in The Technology of Glass and Ceramic, An Introduction, Elsevier Scientific Publishing Company, Amsterdam, Oxford, New York, 1983

97. F. Lin, T. Marier, A. Morrone, and S. Nutt, pp. 323 in High Temperature/High Performance Comp., Edited by F. D. Lemkey et al, Mater. Res. Soc., 1988

98. W. Braue, R. W. Carpenter, and D. J. Smith, J. Mater. Sci., **25**, 2949 (1990)

99. P. F. Becher, E. R. Fuller, Jr., and P. Angelini, J. Am. Ceram. Soc., **74** [9] 2131-35 (1991)

VITA

Yiqun Pan was born in Shanghai, China on July 6, 1957. She attended elementary and secondary schools in that city and was graduated from Yi Shan High School in February 1975. From 1975 to 1977 she studied in the Technical School of Shanghai Capacitor Factory. After the school study she worked in the factory as an inspector of product quality control.

In February 1978 she entered Shanghai Jiao Tong University, and in February 1982 she received a Bachelor of Engineering degree in Precision Instrument.

In the spring of that year she was employed as a lecturer in the Department of Mechanical Engineering of the Staff and Worker's College of Shanghai Light Industry.

After two years working in the college, in summer 1984 she went to Shanghai Jiao Tong University, Branch, working as a research associate in Department of Metallic Materials and Technology.

In August, 1990, she entered the graduate school of the University of Tennessee, Knoxville. She received the Master of Science degree with a major in Materials Science and Engineering in December 1992.

The author is a member of honor society of Phi Kappa Phi and a student member of ASM International and The American Ceramic Society.